Analysis of Radiation Mechanism and Polarizing Properties of Metamaterials

by

Madhusudhan Nikku

Submitted to the Department of Civil and Environmental Engineering
in partial fulfillment of the requirements for the degree of

Master of Science

at the

MASSACHUSETTS INSTITUTE OF TECHNOLOGY

September 2004

Author .....
Department of Civil and Environmental Engineering
July 25, 2004

Certified by ....
Jin Au Kong
Professor, Department of Electrical Engineering and Computer Science
Thesis Supervisor

Certified by ....
Chiang C. Mei
Professor, Department of Civil and Environmental Engineering
Thesis Reader

Accepted by ....
Heidi M. Nepf
Chairman, Department Committee for Graduate Students

Analysis of Radiation Mechanism and Polarizing Properties of Metamaterials

by

Madhusudhan Nikku

Submitted to the Department of Civil and Environmental Engineering
on July 27, 2004, in partial fulfillment of the
requirements for the degree of
Master of Science

Abstract

Metamaterials are media have a negative permittivity (ϵ) or a negative permeability (μ) or both. Metamaterials promise tremendous advances in lensing applications, antenna technologies and the like. In the present research, the radiation mechanism of metamaterial composites made up of pairs of S-shaped structures (also known as S-rings) is studied in detail. Numerical simulations using the Ansoft HFSS ^{TM} software package, lead to an understanding of the currents induced on a single S-ring due to a plane wave excitation. The current density observed along a single ring is expressed as a periodic function of the distance along it, and the vector current moment is determined. The far field radiation for a pair of S-rings is determined using this vector current moment. The refraction of a plane wave travelling from a prism made up of S-rings into free-space is studied. In order to determine the far field radiation due to a prism made up of S-rings, the array factor specific to the prism structure is determined first. This array factor coupled with the radiation pattern due to a single ring gives the pattern due to the prism. The radiation pattern of a prism of S-rings, which shows the refraction direction, is determined for two cases with prism angles of 28^o and 39^o.

Metamaterials with negative uniaxial permittivities, and positive isotropic permeabilities, display unusual polarizing capabilities. The polarizing capabilities of such metamaterials are also studied in the present work. The performance characteristics of a metamaterial polarizer are compared to those of existing O-type and E-type polarizers. The proposed metamaterial polarizer has a uniaxial permittivity tensor with a negative permittivity along the optic axis and a positive isotropic permeability. The characteristics used as a basis for comparison are: 1. Leakage of light (transmittance) through a pair of crossed-polarizers, and 2. Fresnel coefficients of a single polarizer. The expressions for the transmittance and the Fresnel coefficients are obtained analytically using the kDB method. A novel procedure to determine the angles of transmission of the ordinary and extraordinary waves through a uniaxial slab is developed, along with the procedures for validation. The viability of enhancing the

performance of polarizers by using metamaterial media is investigated.

Thesis Supervisor: Jin Au Kong
Title: Professor, Department of Electrical Engineering and Computer Science

Acknowledgments

Puzzled by the myriad manifestations of Nature, I chose at a point to stand still. Standing thus, I urged upon Time to take me along and it did. I owe any success that I ever had to that dynamism that is latent in Nature.

I am greatly indebted to my advisor Professor Jin Au Kong, who introduced me to research in Electromagnetics and gave me the opportunity to delve into this exciting field of Metamaterials. He has been a great teacher and advisor. The intellectual freedom that he allowed in the various facets of research, and life in general, proved very valuable to me.

I would like to wholeheartedly thank Dr. Tomasz M. Grzegorczyk for his continuous guidance over the whole period of the present work. His patience and forbearance during the different stages of my research experience were inexplicably praiseworthy. Working with him has been a great experience. I would also like to thank Dr. Bae-Ian Wu for his encouragement and support during this period. His regular advice on scientific methodology added significant value to my attitude towards research.

I have greatly benefitted in various ways from the excellent past and present members of the group, Dr. Benjamin E. Barrowes, Dr. Christopher D. Moss, Dr. Joe Pacheco, Jie Lu, Jianbing Chen, Xudong Chen, Weijen Wang, Zachary M. Thomas, Brandon A. Kemp, William F. Herrington and Beijia Zhang.

I would like to thank Dr. John T. Germaine for being my academic advisor during this period, and Professor Chiang C. Mei, for being my Thesis Reader.

Contents

List of Figures

List of Tables

Chapter 1

Introduction

1.1 Historical Background

There has been a recent upsurge of interest in the electrodynamics of media having negative permittivities and permeabilities, in selective frequency bands in the microwave regime [1]. These media, popularly known as metamaterials, posses a negative refractive index (n) in the spectral region where both the permittivity (ϵ) and permeability (μ) are negative. Also known as Left-Handed Media (LHM), a wave propagating in one such medium has its phase reversed such that the wave vector, the Electric Field and the Magnetic Field form a Left-Handed (LH) triad. As a consequence, the wave vector and the Poynting vector are opposite in direction for an isotropic LHM. The prospect of realising a negative index of refraction, and the many other interesting phenomena that LHM promise, opens up wide ranging applications that were hitherto considered impracticalities.

LHM were first studied by Victor G. Vesalago in 1968 [3]. Veselago studied a hypothetical LHM, noting that ϵ and μ can be simultaneously negative in a particular frequency band, only if they are dispersive. Given the fact that there was no such material known at that time, the study in [3] was one of predominantly theoretical interest, albeit a highly imaginative one. Assuming an hypothetical LHM, however, the said work elucidated some of the most important consequences of such media

as reversed Doppler effect, anomalous refraction phenomena, etc, for the first time. The frequency dispersion was proposed to be Drude-type for both ϵ and μ. The existence of plasmas having a Drude-type effective ϵ was known for long. But the justification for the possibility of a magnetic analogue, as presented in [3], had neither a firm theoretical basis nor any experimental verification. The non-existence of such a media with simultaneously negative ϵ and μ, precluded any progress in this direction for about the next 30 years.

However, with the advent of improved fabrication methods and novel artificial electromagnetic structures like photonic crystals, etc., curiosity about negative ϵ and μ revived in the 90's. Negative permittivities were known, for long, for plasmas in solid state [4][5]. Surface plasmons in metals give rise to a Drude-type dielectric function leading to negative permittivities at frequencies in the optical range. However, at lower frequencies, high losses come into play and the negative ϵ effect is nullified. This fact, along with the difficulty of having magnetic resonances at high frequencies, posed a serious impediment to realising LHMs. One of the first attempts to overcome this limitation was made by Pendry et.al (1996)[6]. Their work proposed a geometrical scheme in which the plasma frequency of a metallic structure could be obtained in the Microwave regime. They considered an assembly of thin metallic wires, of the order of 1μm cross-sectional radii, which constrained the plasmons to oscillate along the wires. The plasma frequency in a metal is, in general, a function of the number density and mass of the oscillating electrons. However, by constraining the electrons to the thin metallic wire assembly, their effective number density is greatly reduced and the effective mass enhanced. This synergism leads to a reduced plasma frequency for the entire structure. The plasma frequency, as shown in [6], is dependent only on the macroscopic geometrical parameters of the structure, namely, the radius of the wires and the lattice spacing of the assembly. Considering a lattice of aluminium wires of 1μm radius and 5mm spacing, a plasma frequency of 8.2 GHz was obtained in [6] and [7]. Numerical simulations and experimental verification of the results confirmed the theory in [7]. Thus the prospect of obtaining negative epsilon at lower frequencies

was rendered possible. However, the negative μ still remained elusive at that point. .

A composite material which could give a desired magnetic response was the goal. As long as the unit cell of the composite is small compared to the wavelength of the electromagnetic radiation, the composite can be considered to be homogenous. It is then just a matter of determining the effective permeability of the composite material in terms of the parameters of the unit cell, just as our conventional notion of permeability of a material medium is a definition in terms of the properties of the atomic constituents. This was the concept on which Pendry et. al (1999) built upon, culminating at a landmark metallic geometry which promised a negative permeability in the microwave regime. Starting with an array of thin metallic cylinders, and working through some examples of magnetic microstructures, they finally derived the effective permeability due to a split ring structure [8]. The final structure was a three dimensional stack of split ring resonators (SRRs), each unit cell measuring about 1sq.cm. The effective permeability of such a system was derived to be resonant in form. An SRR could be decomposed into a set of capacitative, inductive and resistive elements. An incident magnetic field induces currents in the circular loops of the rings, thereby forming an RLC circuit. The Inductance, Capacitance, and the Resistance of the circuit were purely a function of the frequency and the geometrical parameters. Thus, with an appropriate choice of the parameters, a resonance frequency in the desired range could be obtained. Proceeding thus, a resonant frequency of 13.5 GHz was obtained. This marked the onset of artificial electric and magnetic microstructures, combinations of which were capable of obtaining negative ϵ and μ in the microwave range, simultaneously.

1.2 Basic Principles

Before delving into deeper ramifications of the LH behavior of these artificial media, it is pertinent to ponder over some of the basic principles guiding this behavior. In as much as the negative refractive index is concerned, all we are concerned about is the possibility of a negative ϵ and a negative μ, simulataneously. However, the forms of

the permittivity and permeability functions that have been realised practically, and the conditions that need to be met to obtain the same, form an interesting aspect of this area.

1.2.1 Negative Permittivity

Negative ϵ in conventional LHMs is obtained by an array of thin metallic wires, of specific dimensions [6]. A typical set-up of the rods in free space is shown in Figure 1-1. For a plane wave excitation, with the Electric Field ($\bar{E}$) vector along the wires, the free charges in the metal are set to oscillate along them. By keeping the cross-section of the wires very small, the effective density of the charges in the lattice space is greatly reduced and the effective mass enhanced. The plasma frequency is given by,

$$\omega_p^2 = \frac{ne^2}{\epsilon_o m_{eff}}$$

where, n is the number density of the charges (plasmons) and m_{eff} is the effective mass of the charges. Thus, by decreasing the density and increasing the effetive mass, the plasma frequency can be lowered. Theoretical analyses and experimental observations support this phenomenon. [6] [9]. It has also been verified that such a effective medium has an effective permittivity given by:

$$\epsilon = \epsilon_o(1 - \frac{f_{ep}^2}{f(f + i\gamma/2\pi)})$$

where, $f_{ep} = \omega_p/(2\pi)$ is the plasma frequency and γ is inversely proportional to the conductivity of the medium and has units of frequency. A plot showing $\epsilon(f)$, for $\gamma = 0GHz$ is shown in Figure 1-2.

Apart from wire structures which give a negative effective permittivity, some other structures have recently been proposed and experimentally verified. Two of the most recent ones are the Omega structure [11] and the S structure [12]. All these structures have thin metallic components parts of which are parallel to the incident Electric

Field. Thus, common to all LH structures is the underlying phenomenon that an electric field parallel to thin metallic structures constrains the charges to oscillate along the structures giving rise to a plasma behavior, and hence a plasma-type dielectric function.

1.2.2 Negative Permeability(μ)

Negative μ in LHMs is obtained by an array of metallic split rings, commonly known as Split Ring Resonators (SRRs). A typical set-up of periodically spaced SRRs is shown in Figure 1-3. Also shown in the figure, is the wave incidence direction leading to a negative permeability. The rings are in the plane of the paper and the Magnetic Field ($\bar{H}$) is directed out of the plane of the paper. A varying magnetic field in this direction induces currents in the loops of the rings. The geometry of the rings leads to effective capacitances and resistances in the path of the current [8]. These capacitative and resistive elements along with the current loop form an RLC circuit. The resonant frequency of this circuit depends purely on the geometry of the metallic structure, and has been succesfully realized in the microwave regime.

The effective permeability of such a structure is given by,

$$\mu = \mu_o(1 - \frac{f_{mp}^2 - f_{mo}^2}{f^2 - f_{mo}^2 + i\gamma/2\pi})$$

where, f_{mp} is the magnetic plasma frequency, f_{mo} is the magnetic resonant frequency and γ is the loss component having units of frequency. A plot showing the resonant behavior of the permeability is also shown in Figure 1-2, with $\gamma = 0GHz$.

1.2.3 LHM Geometries

As seen in the previous sections, thin wire shaped metallic elements (rods) parallel to the $\bar{E}$ and metallic loops in the plane perpendicular to the $\bar{H}$ of an incident plane wave give rise to a plasma-type ϵ and a resonant μ respectively. The overlapping frequency band, where ϵ and μ are simultaneously negative, is the LH band. Thus

combinations of rings and wire elements have been widely used to realize LHMs in the microwave regime [9] [10]. Figure 1-4 shows a typical set-up of a ring-rod combination with the proper incidence which gives rise to LH behavior.

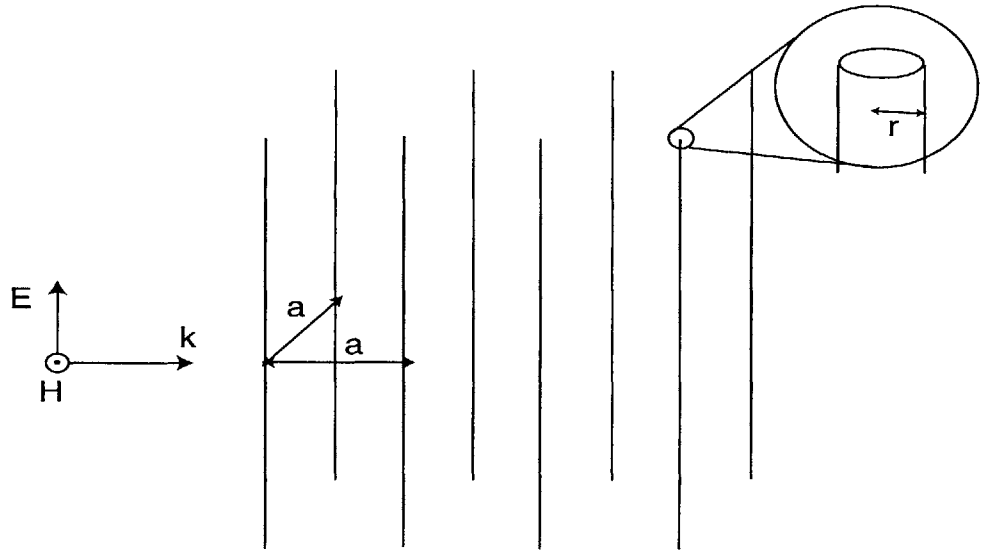

Figure 1-1: **Array of thin wires in free space leading to negative epsilon (a = few millimeters and r = few microns)**

Apart from the standard SRR - rod combination, which were traditionally used to obtain LHM, new structures have been introduced in the recent past to achieve the same purpose. Figure 1-5 shows an array of Omega shaped rings forming an LHM. In this case, two omega rings are placed one behind the other and each ring being a mirror image of the other. Figure 1-6 shows an array of S shaped rings forming an LHM. As in the case of the omega rings, here also the two S-rings are placed one behind the other as mirror images.

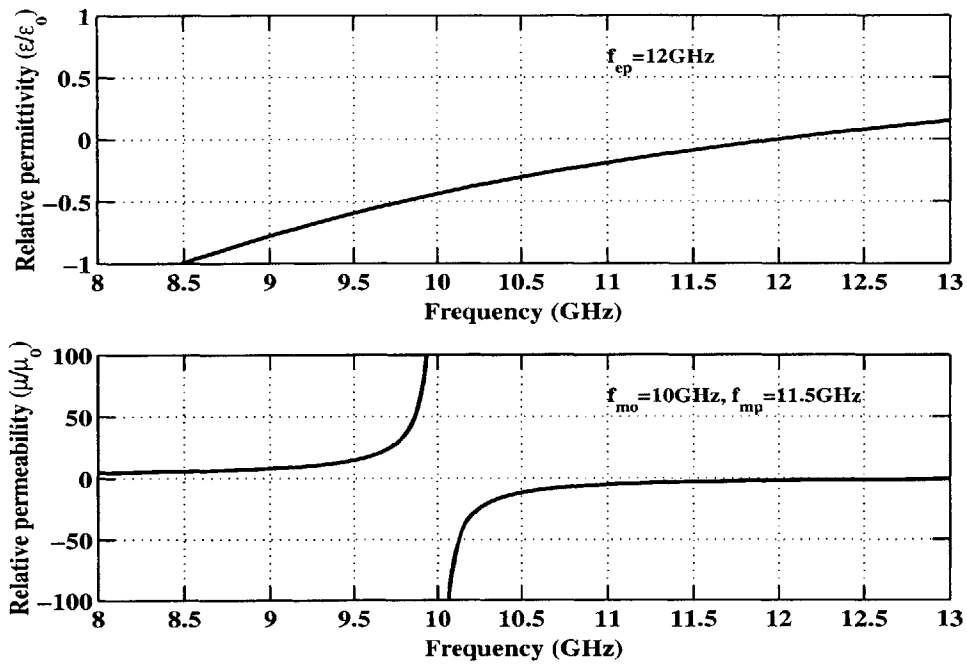

Figure 1-2: **Typical Permittivity and Permeability functions for LHMs**

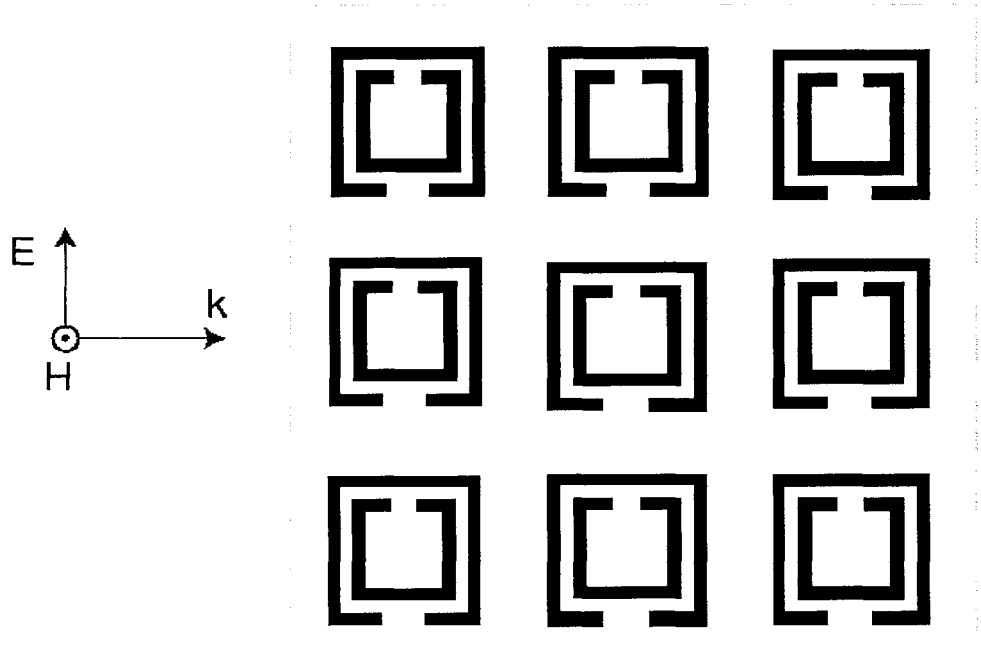

Figure 1-3: **An array of Split Ring Resonators (SRRs) leading to a negative permeability (Unit cell is of the order of a few millimeters, ex: 4mm $\times$ 4mm)**

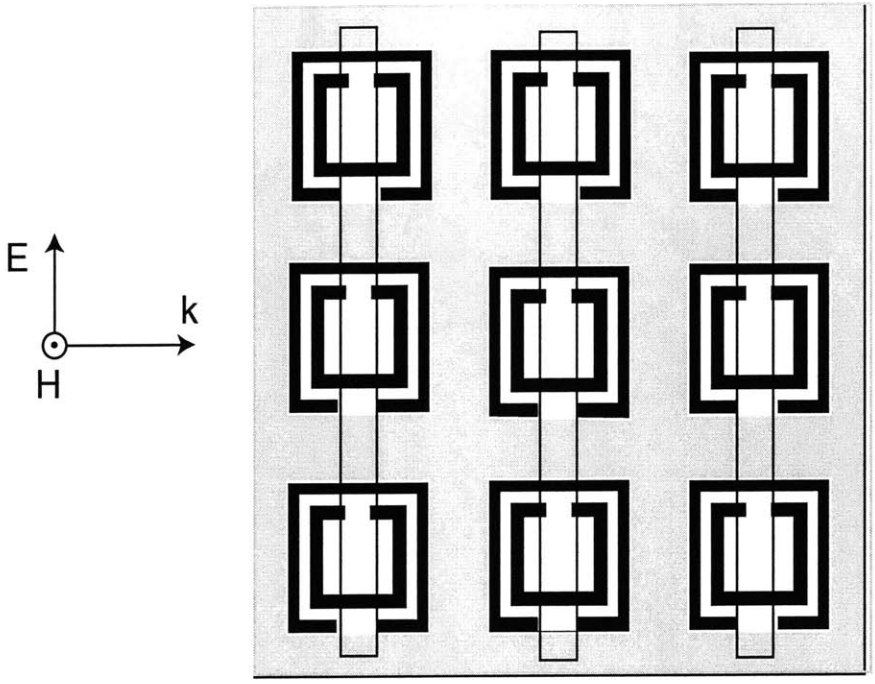

Figure 1-4: **A set-up of metallic rods and split rings on a dielectric substrate forming an LHM**

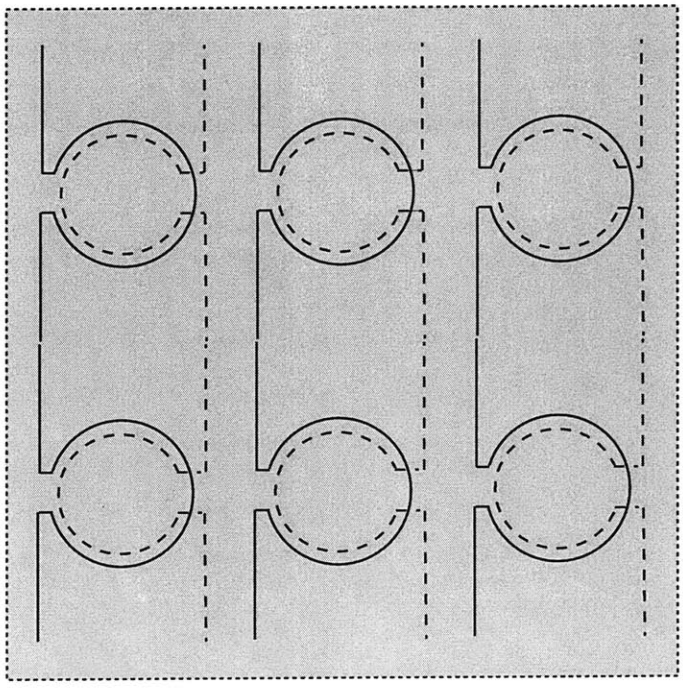

Figure 1-5: **A set-up of Omega rings on a dielectric substrate forming an LHM**

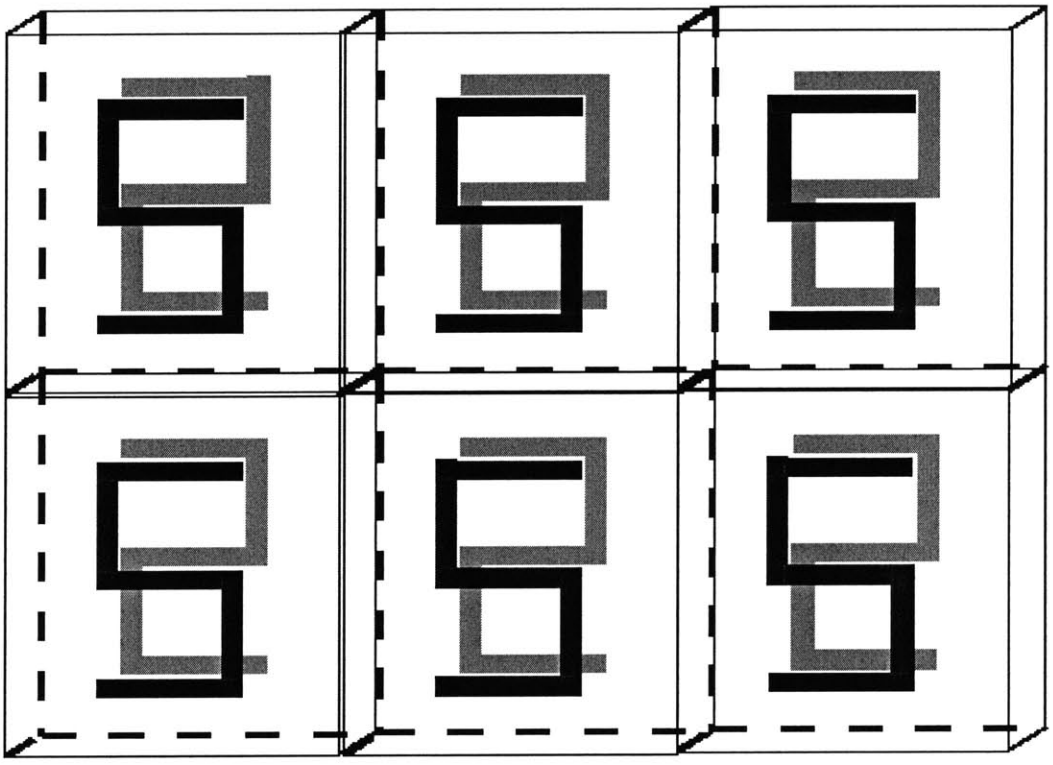

Figure 1-6: **A set-up of S rings forming an LHM. Each unit cell contains two S shaped rings printed on the two sides of a dielectric substrate**

Chapter 2

Radiation due to S shaped SRR

2.1 Introduction

Conventional Left-handed materials have been fabricated using composites of metallic rings and rods. The rings, commonly known Split Ring Resonators (SRR) [8], lead to a resonant effective permeability (μ). And, the rods, which are thin metallic wires, lead to a plasma type effective permittivity (ϵ) [6]. In the overlapping frequency band, where ϵ and μ are both negative, a negative refractive index (n) is observed leading to the well-known Left-Handed (LH) behavior of the composite material. It was recently demonstrated that S-shaped metallic structures (S-rings) exhibit LH characteristics equivalent to an SRR-rod combination [2]. And, negative refraction in a prism made of such structures was experimentally verified [12] , in the frequency band roughly between 15GHz-20GHz, depending on the physical dimensions of the setup.

An S shaped SRR consists of two parallel S-rings oriented oppositely as shown in Figure 2-1. A varying magnetic field perpendicular to the parallel plane of the rings induces currents along the rings. These currents along with the resistive, capacitative and inductive elements imposed by the geometry of the rings, lead to a resonant magnetic response similar to that in a conventional SRR. Also, an incident electric field along the longer sides of the rings, in the parallel plane, induces a plasma type electric response similar to that in an array of thin rods (the conventional rod medium).

In this section, the radiation characteristics of composites made up of such S-shaped SRRs are studied in detail. Numerical simulations using the Ansoft HFSS ^{TM} numerical package lead to an understanding of the currents induced due to a plane wave excitation on each of the two S rings in an SRR. The incident plane wave is a TEM mode at 17GHz, with the Electric Field vector in the plane of the ring and the magnetic field vector perpendicular to the plane of the ring. The values of the surface current density (J) are obtained at discrete positions along each S-ring. A discrete fourier transform of this data allows one to express J as a fourier expansion. This facilitates an analytic expression for J along a ring as a function of the normalized distance along the ring. The current density thus obtained is used to determine the vector current moment due to the ring [2]. The far field radiation due to the ring is then determined using this vector current moment. The radiation pattern to a single S-ring is found to be symmetric in nature and resembles a radiation pattern due to a combination of dipoles stacked along the segments of the S-ring with the given current distribution.

In order to determine the far field radiation due to a composite made up of S-rings, the array factor specific to the composite structure is determined first. This array factor coupled with the radiation pattern due to a single ring gives the pattern due to the composite. The progressive phase increment between rows of the array are obtained from HFSS ^{TM} simulations of a slab of S-shaped SRRs. Prisms of S-rings with different prism angles and dimensions are studied. It is observed that the characteristic negative refraction of the composite is observed considering the edge elements of the prism, and using a negative progressive phase shift. On the other hand, considering all the prism elements leads to substantial diminution of the distinct lobes and a radiation pattern concentrated parallel to the incidence direction is observed, showing no LH behavior whatsoever.

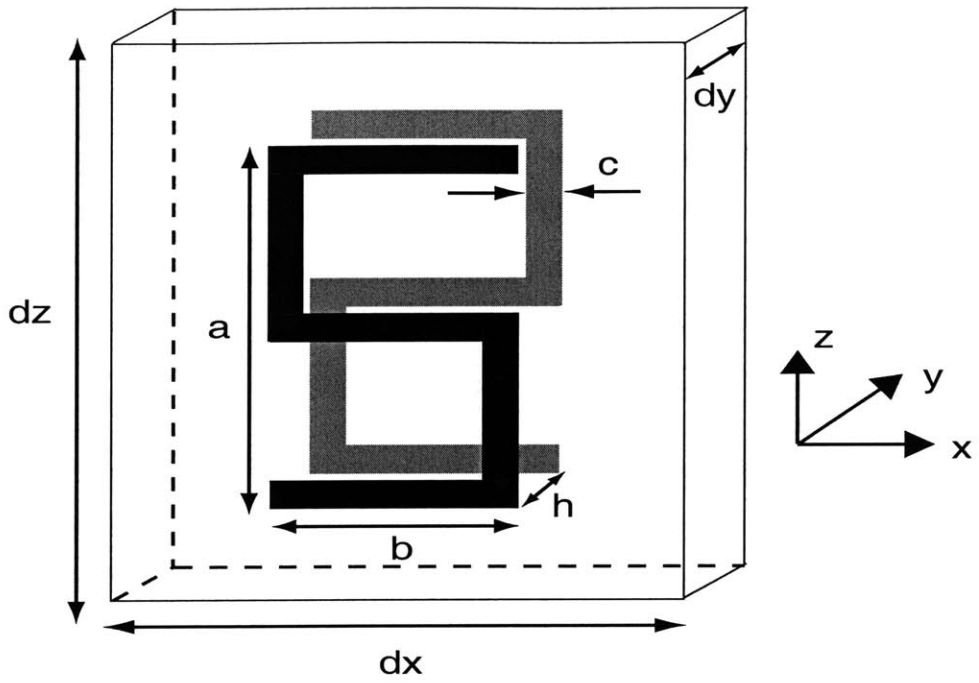

Figure 2-1: **The S-shaped SRR (Dimensions (in mm, not to scale) : a= 5.2, b=2.8, c=0.4, h=0.5, dx=4, dy=2.5, dz=5.4)**

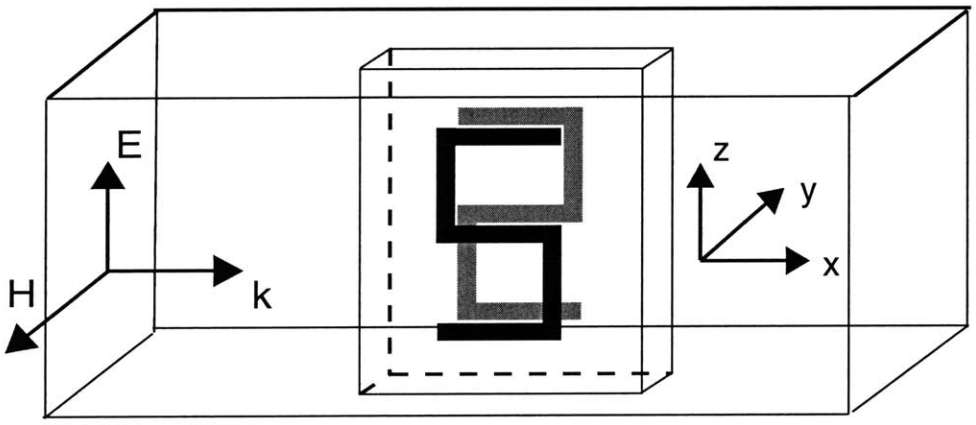

Figure 2-2: **Set-up of a unit cell of S-rings inside a rectangular Waveguide**

2.2 S-parameters and Effective Refractive Index

The simulation setup of an S shaped SRR inside a rectangular waveguide is shown in Figure 2-2. The boundaries of the waveguide parallel to the rings are assigned to be Perfect Magnetic Conductors (PMC) so as to facilitate a TEM mode as the fundamental mode. The incidence is a plane wave with a frequency of 17GHz, which lies in the resonant band. The dimensions of the unit cell containing the two rings are shown in Figure 2-1. The setup was simulated using HFSS ^{TM} .

Two cases were studied corresponding to one and two S-rings placed along the propagation direction in the waveguide. These two cases correspond to increasing thickness of the effective medium made up of the S-rings, and we denote them as one-layer and two-layer respectively; a layer corresponding to one SRR in the wave guide along the propagating direction.

With the set up as mentioned above, the S-parameters, S11 and S21 were obtained for the two cases. As is well-known, the magnitudes of S11 and S21 correspond to the reflection and transmission coefficients of the medium, respectively. Figures 2-3, 2-4 show the S-parameters in the two cases. It can be observed in the figures that there is a band of high transmission around 17 GHz and the transmission falls off rapidly for other frequencies. It can also be seen that as the thickness of the effective slab, i.e the number of layers, is increased the peak band gets slightly wider.

Such a peak in the transmission spectrum for an LH Medium corresponds to the resonant band where the refractive index (n) is negative. For frequencies lying outside this band, only one of ϵ and μ are negative. This leads to an imaginary refractive index which causes significant attenuation of the incident wave and hence very low transmission. However, it should be noted that obtaining such a peak in the transmission spectrum does not always imply LH behaviour. The possible LH behaviour can be verified by retrieving the material parameters of the medium, namely n, ϵ and μ, from the S-parameters.

Some of the first studies on the retrieval of, permittivity (ϵ) and permeability (μ),

for LH media can be found in [18],[19] and [20]. The general approach followed in these studies was to obtain the n and the impedance, z, of the material medium from the S-parameters and then retrieve the ϵ and μ from the n and z, using $\mu = nz$ and $\epsilon = n/z$. However this approach has been known to be inaccurate in certain cases. These associated problems were studied in greater detail in [17]. Xudong et. al. have developed a robust method to overcome the problems of the previous method and to obtain the material parameters from the S parameters in [17]. This approach has been used in the present work to retrieve the material parameters of the medium composed of S-shaped SRRs, from the S-parameters shown in Figures 2-3 and 2-4.

Figures 2-5 and 2-6 show the frequency dependant refractive index (n) for the cases with one and two layers respectively. It can be seen that the refractive index is negative in the frequency band ranging approximately from 12GHz to 20GHz. This is a confirmation of LH behaviour of the effective media. It can be observed that the figures are nearly identical, confirming the accuracy of the retrieval procedure.

Also, the high transmission regions in the S-parameter plots fall within this band, and peaking at 17GHz (as in Figures 2-3 and 2-4). The refractive index at 17GHz, i.e resonance, as obtained from the retrieval (Figures 2-3 and 2-4) is found to be -1.59. This is the effective Refractive Index (n) of the S-ring medium at resonance.

In what follows, the surface current densities on the S-rings in the wave guide setup are studied. These currents are then used to determine the radiation pattern of an S-ring prism. The angle of refraction obtained with such a prism is used to determine the effective n of the S-ring medium. The n thus obtained is compared with the n obtained in the present section.

2.3 Current Modes

Solving the setup as shown in Figure 2-2, with HFSS ^{TM}, with the appropriate mesh refinement and other numerical parameters, allowed the computation of J for each ring along a trace running along the centerline of the ring. A plot of J thus obtained

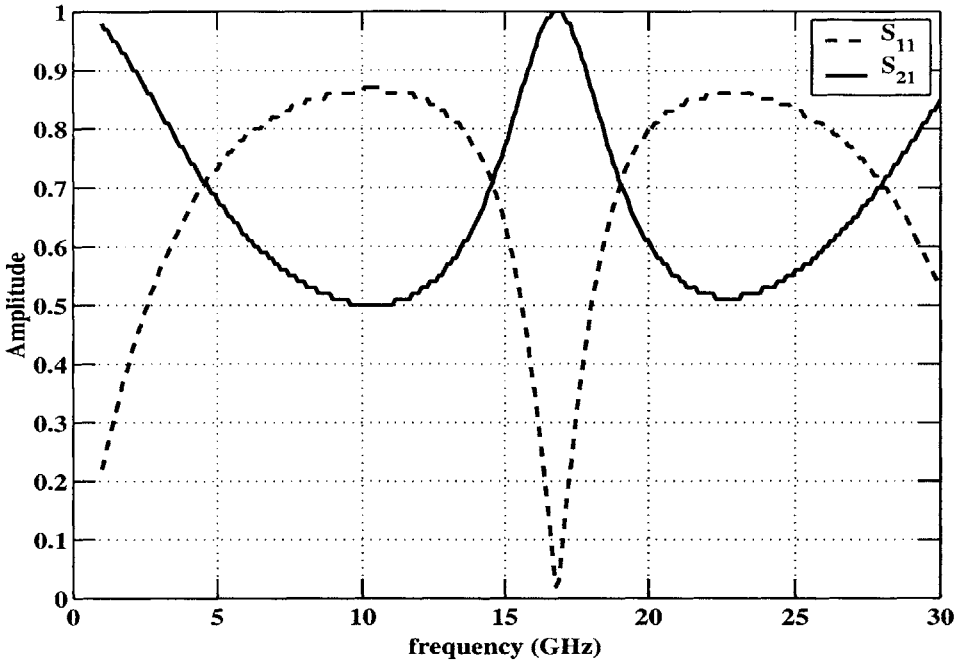

Figure 2-3: **S-parameters for one layer of S-rings with dimensions as shown in Figure 2-1**

is shown in Figure 2-7.

The plots of J for the two rings suggest that J is a periodic function of the normalized distance along the ring (l) i.e. $J = J(l)$, with boundary conditions $J(0) = J(1) = 0$. Assuming J(l) is a continuous function, one can try to expand J in terms of its Fourier components as:

$$J(l) = a_o + \sum_{n=1}^{\infty}(a_n sin(2\pi nl) + b_n cos(2\pi nl)) \tag{2.1}$$

where,

$$a_o = \int_0^1 dl J(l)$$

$$a_n = 2\int_0^1 dl J(l) sin(2\pi nl)$$

$$b_n = 2\int_0^1 dl J(l) cos(2\pi nl)$$

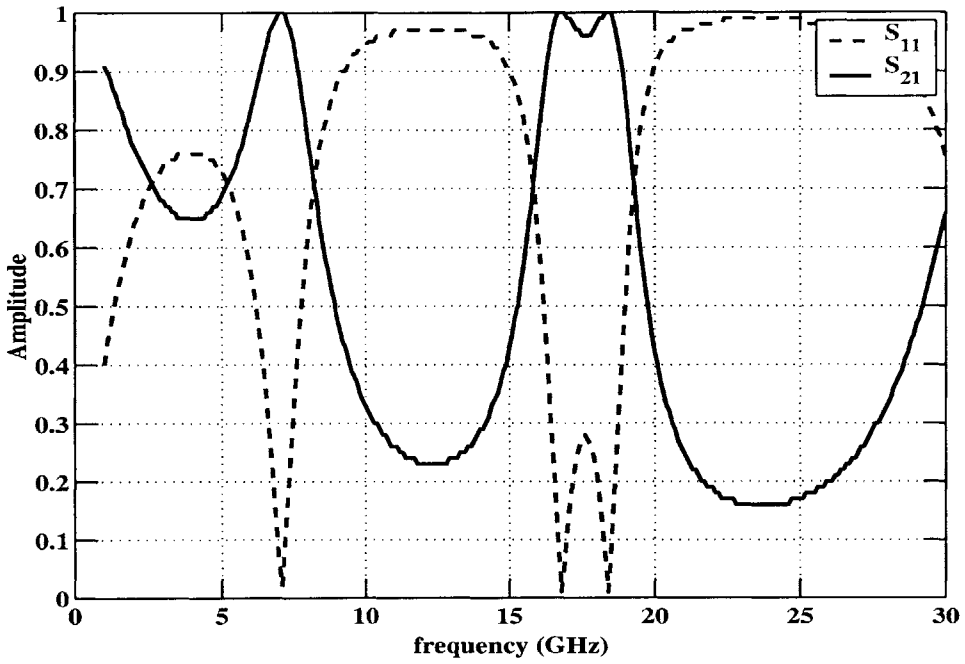

Figure 2-4: **S-parameters for two layers of S-rings with dimensions as shown in Figure 2-1**

In the present case, however, we have a discrete set of data for each ring. The Fourier components for this situation can be obtained using the Fast Fourier Transform method. A MATLAB function was used to implement this. Figure 2-8 shows a plot of the actual J along with 21 Fourier components, for the front ring. Figure 2-9 shows the corresponding plot for the back ring.

As can be seen from the plots, in each case there is one dominant mode corresponding to n=1 in the expansions. Thus the total J on each of the rings can be approximately represented using a single dominant mode, although the next few significant modes could also be included in the representation. Thus we have an analytical expression for the currents along the rings. This facilitates the analytical derivation of the radiation fields due to the pair of rings, as in the following section.

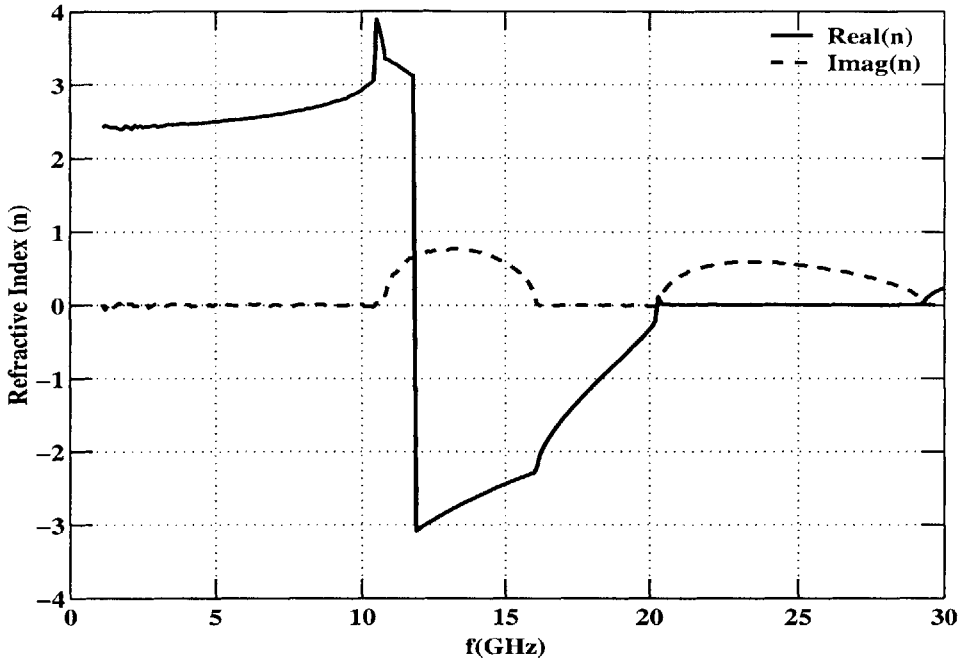

Figure 2-5: **Retrieved Refractive Index for one Layer of S-rings with dimensions as shown in Figure 2-1**

2.4 Radiation due to S shaped SRR

The set-up of an S-ring geometry is shown in Figure 2-1. Each ring is in the x-z plane with the longer side of the ring along the z-axis and the shorter side along the x-axis. The ring can be viewed as five distinct rectangular metallic elements each of which is either along the x-axis or along the z-axis. As mentioned in (2.1), the current density along the ring can be expressed as a sum of the fourier modes. We can thus express the current density along each ring as:

$$J(s) = \sum_{n=1}^{N} a_n sin(\frac{2n\pi s}{L}) \tag{2.2}$$

where, N is the number of significant modes, s is the length along the ring and L is the total length.

The current density along each segment, directed predominantly either along the x-direction or along the z-direction, can be expressed as:

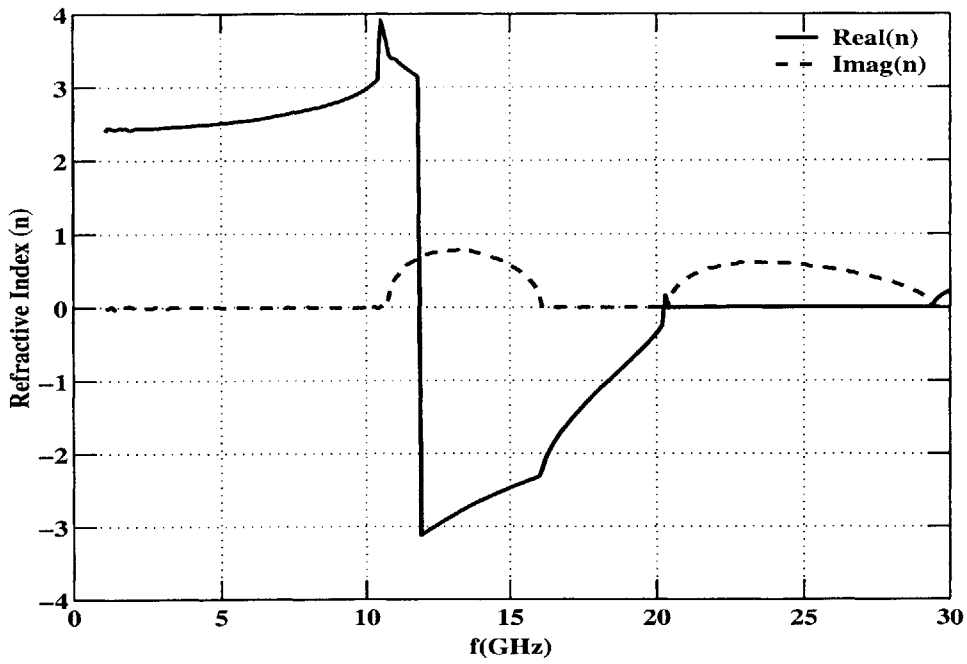

Figure 2-6: **Retrieved Refractive Index for two Layers of S-rings with dimensions as shown in Figure 2-1**

$$\bar{J}_x = \hat{x} \sum_{n=1}^{2} a_n sin(\frac{n\pi}{L}(b+x))\delta(y-y_1)\delta(z-z_1)$$
$$\bar{J}_z = \hat{z} \sum_{n=1}^{2} a_n sin(\frac{n\pi}{L}(b+z))\delta(y-y_1)\delta(x-x_1) \tag{2.3}$$

where, $\delta(y)$ is the Dirac Delta funtion and b is a real scalar quantity determined by the positions of end points of the segment under consideration.

In order to determine the radiation due to a current carrying element, it is convenient to first determine the vector current moment [1] given by:

$$\bar{f}(\theta,\phi) = \int\int\int d\bar{r}'\bar{J}(\bar{r}')e^{-i\bar{k}\cdot\bar{r}'} \tag{2.4}$$

For the present problem, we need to determine the vector current moment ($\bar{f}$) for the current distribution given by (2.3). Let us consider a typical current distribution of the form:

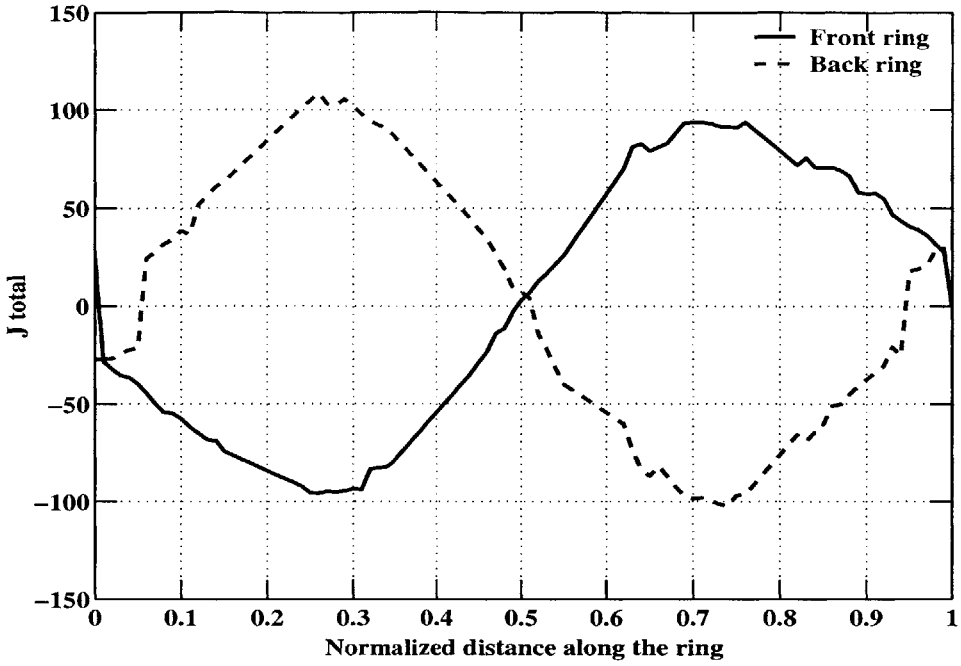

Figure 2-7: **Surface Current density (J) on the front and back rings of the S-shaped SRR with dimensions as shown in Figure 2-1**

$$\bar{J}_{xn} = \hat{x} a_n sin(\frac{n\pi}{L}(b + x'))\delta(y' - y_1)\delta(z' - z_1) \tag{2.5}$$

where, $x' \in [x1, x2]$, i.e the segment of the ring is along the x-axis.

The $\bar{f}$, denoted as $\bar{f}_x$ for this case, can be determined as,

$$\bar{f}_{xn} = \hat{x} f_{xn} = \hat{x} \int \int_{\bar{r}'} \int dx'dy'dz' a_n sin(\frac{n\pi}{L}(b + x'))\delta(y' - y_1)\delta(z' - z_1) e^{-i(k_x x' + k_y y' + k_z z')}$$

$$= \hat{x} a_n e^{-i(k_y y_1 + k_z z_1)} \int_{x_1}^{x_2} dx' sin(\frac{n\pi}{L}(b + x'))e^{-ik_x x'}$$

$$\Rightarrow \bar{f}_{xn} = \hat{x} a_n \frac{e^{-i(k_y y_1 + k_z z_1)}}{n^2\alpha^2 - k_x^2}[ik_x sin(n\alpha(b + x')) + n\alpha cos(n\alpha(b + x'))e^{-ik_x x}]_{x_1}^{x_2} \tag{2.6}$$

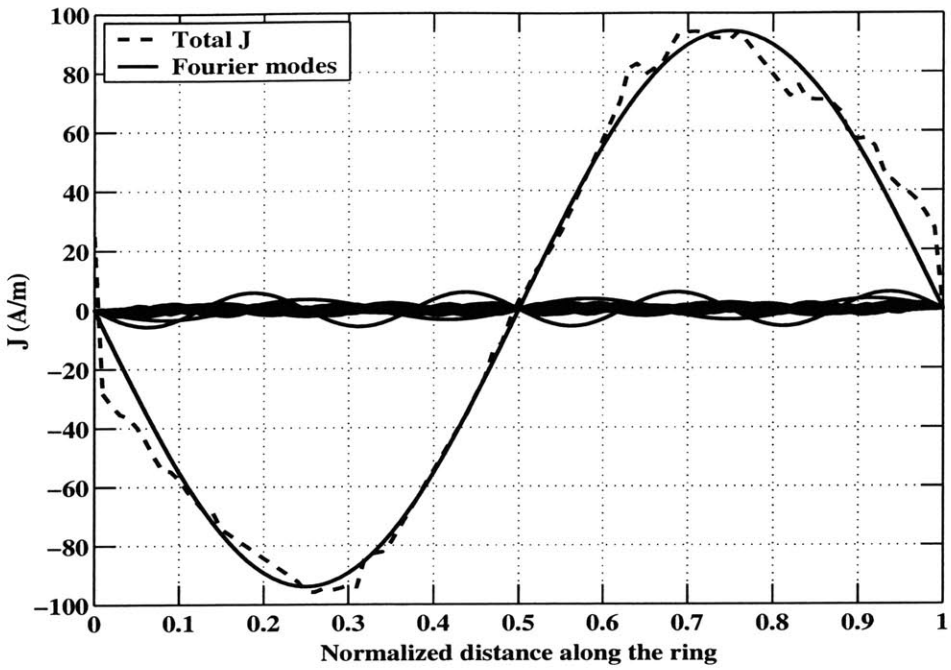

Figure 2-8: **Fourier expansion of J on the front ring of the Unit Cell shown in Figure 2-1**

Thus the total vector current moment including all the fourier modes under consideration, can be expressed as:

$$\bar{f}_x = \hat{x} \sum_{n=1}^{N} a_n \frac{e^{-i(k_y y_1 + k_z z_1)}}{n^2\alpha^2 - k_x^2} [ik_x sin(n\alpha(b + x')) + n\alpha cos(n\alpha(b + x'))e^{-ik_x x}]_{x_1}^{x_2} \quad (2.7)$$

where, $[g(x)]_{x_1}^{x_2} = g(x_2) - g(x_1)$.

Similarly proceeding for the case when the segment is along the z-axis, we have:

$$\bar{f}_z = \hat{z} \sum_{n=1}^{2} a_n \frac{e^{-i(k_y y_1 + k_x x_1)}}{n^2\alpha^2 - k_z^2} [ik_z sin(n\alpha(b + z')) + n\alpha cos(n\alpha(b + z'))e^{-ik_z z}]_{z_1}^{z_2} \quad (2.8)$$

Equations (2.7) and (2.8) give the general forms for the vector current moments along each segment of the ring, depending on whether the segment is along the x-axis or the z-axis. Thus for each segment the $\bar{f}$ vector can be obtained using the known

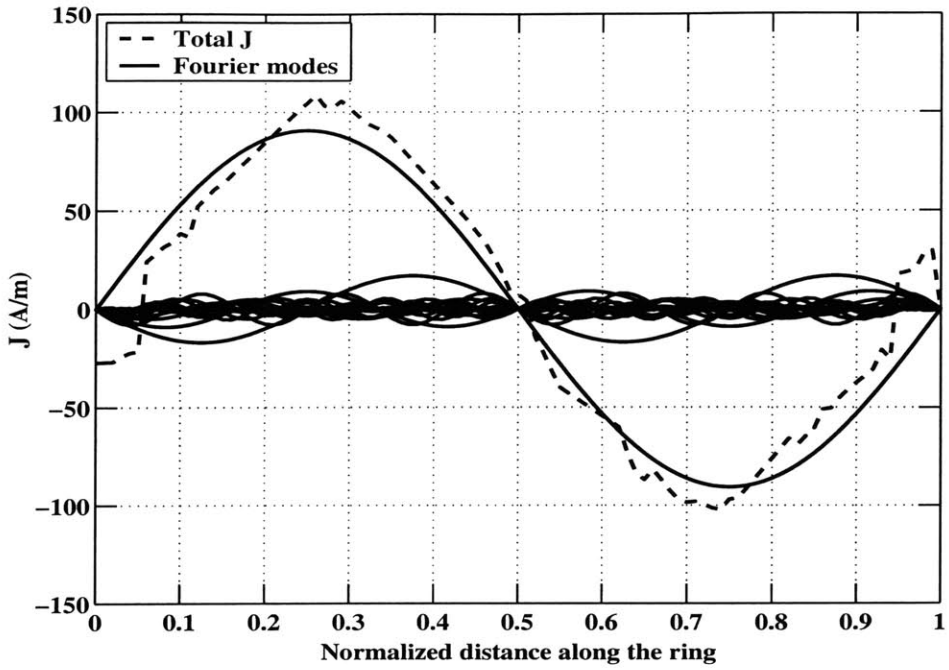

Figure 2-9: **Fourier expansion of J on the back ring of the Unit Cell shown in Figure 2-1**

values of the independent variables, b, y_1 and $[x_1, x_2]$(or $[z_1, z_2]$).

The S ring has five such segments. The total $\bar{f}$ of a single S ring, due to all the segments, is the vector sum of those due to each of the individual segments.

$$\bar{f}_{ring} = \sum_{p=1}^{5} \bar{f}_p \tag{2.9}$$

The S-shaped SRR is composed of two S rings as shown in Figure 2-1. Thus, the total $\bar{f}$ vector due to both the rings can be obtained as:

$$\bar{f} = \sum_{p=1}^{5} [\bar{f}_p^1 + \bar{f}_p^2] \tag{2.10}$$

where, the superscripts 1 and 2 refer to the two rings.

The various values of the independent variables b, y_1 and $[x_1, x_2]$ (or $[z_1, z_2]$) corresponding to the different segments of the two rings are tabulated in Table 2.1.

The $\bar{f}$ vector, thus obtained, is in cartesian coordinates, and is of the form $\bar{f} =$

Front Ring					Back Ring				
$\hat{f}$	b	x_1	y_1	z_1	$\hat{f}$	b	x_1	y_1	z_1
x	0	[0,s]	0	0	-x	-L	[s,0]	d	0
z	s	s	0	[0,s]	-z	s-L	0	d	[0,s]
-x	-3s	[0,s]	0	s	-x	2s-L	[0,s]	d	s
z	3s	0	0	[s,2s]	-z	3s-L	s	d	[s,2s]
x	4s	[0,s]	0	2s	x	-5s+L	[s,0]	d	2s

Table 2.1: **Limits on the J for different sections of the ring (L=total Length of the ring, s=L/5, d=dy=0.5mm)**

$\hat{x}f_x + \hat{z}f_z$. The components f_θ and f_ϕ can be obtained by making a cartesian to spherical transformation.

By noting the transformation,

$$\hat{x} = \hat{r}sin(\theta)cos(\phi) + \hat{\theta}cos(\theta)cos(\phi) - \hat{\phi}sin(\phi)$$
$$\hat{z} = \hat{r}cos(\theta) - \hat{\theta}sin(\theta)$$

we have,

$$f_\theta = cos(\theta)cos(\phi)f_x - sin(\theta)f_z \tag{2.11}$$
$$f_\phi = -sin(\phi)f_x \tag{2.12}$$

where, θ and ϕ are the conventional polar angles in the spherical coordinate system.

Thus we can obtain the far-field radiation for the S-shaped SRR. The radiation pattern can be determined using [2]:

$$\bar{E}(\bar{r}) = i\omega\mu\frac{e^{ikr}}{4\pi r}(\hat{\theta}f_\theta + \hat{\phi}f_\phi)$$

$$\bar{H}(\bar{r}) = ik\frac{e^{ikr}}{4\pi r}(\hat{\phi}f_\theta - \hat{\theta}f_\phi) \tag{2.13}$$
$$< \bar{S} >= \hat{r}\frac{1}{2}\sqrt{\frac{\mu}{\epsilon}}(\frac{k}{4\pi r})^2(|f_\theta|^2 + |f_\phi|^2)$$

2.5 Array Pattern Formulation

2.5.1 Vector Current moment for an arbitrary unit cell

A unit cell (refered to as an '*element*' henceforth) consisting of a pair of S-rings and a substrate is shown in Figure 2-1. The local co-ordinate system(LCS) of the unit cell is shown in Figure 2-10 with primed vectors. The surface current density ($\bar{J}$) on the rings, as developed in the previous sections, can be expressed in terms of the local position coordinates. Let us consider an element with local origin at a position $P_0(x_0, y_0, z_0)$ in the global coordinate system (GCS). Let the position P_0 be denoted by the position vector, $\bar{r}_0$, in the GCS. We denote any arbitrary point (P) in the source region (i.e. in the element) by the position vector $\bar{r}'$ in the GCS. Then, the position vector of the point P in the LCS is given by $\bar{r}'_0 = \bar{r}' - \bar{r}_0$, as shown in Fig.3. Therefore, $\bar{J} = \bar{J}(\bar{r}') = \bar{J}(\bar{r}'_0) = \bar{J}(\bar{r}' - \bar{r}_0)$.

The vector current moment due to an element at P_0 is given by:

$$\bar{f}_0 = \int\int_{\bar{r}'}\int d\bar{r}'\bar{J}(\bar{r}')e^{-i\bar{k}\cdot\bar{r}'} = \int\int_{\bar{r}'}\int d\bar{r}'\bar{J}(\bar{r_0}')e^{-i\bar{k}\cdot\bar{r}'} \tag{2.14}$$

Noting that $\bar{r}'_0 = \bar{r}' - \bar{r}_0$, we have:

$$\bar{f}_0 = e^{-i\bar{k}\cdot\bar{r}_0}\int\int_{\bar{r}'_0}\int d\bar{r}'_0\bar{J}(\bar{r_0}')e^{-i\bar{k}\cdot\bar{r_0}'} \tag{2.15}$$

Analogous to the above case, we can also consider another element at a point P_1 given by the position vector $\bar{r}_1$ in the GCS. Then the position vector of an arbitrary point P in the LCS is given by $\bar{r}'_1 = \bar{r}' - \bar{r}_1$. Then, proceding similarily as above, the vector current moment due to an element at P_1 is given by:

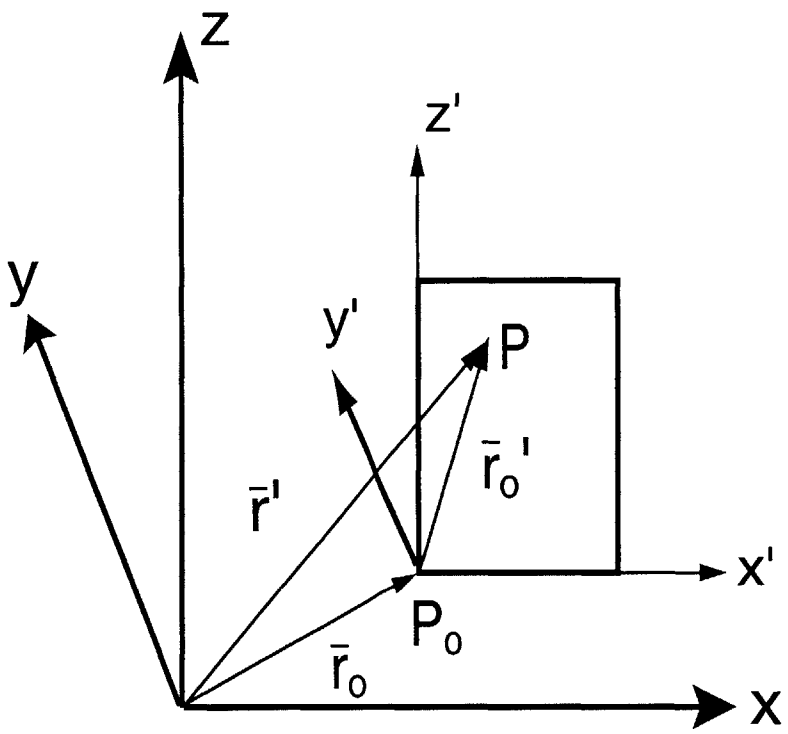

Figure 2-10: **Local and Global Coordinate systems of a Unit Cell**

$$\bar{f}_1 = e^{-i\bar{k}.\bar{r}_1} \int \int_{\bar{r}_1'} \int d\bar{r}_1' \bar{J}(\bar{r}_1') e^{-i\bar{k}\cdot\bar{r}_1'} \tag{2.16}$$

By making a change of variables and noting that the local geometry of all unit cells are indentical, we have:

$$\bar{f}_1 = e^{-i\bar{k}\cdot\bar{r}_1} \int \int_{\bar{r}_0'} \int d\bar{r}_0' \bar{J}(\bar{r}_0') e^{-i\bar{k}\cdot\bar{r}_0'} = e^{-i\bar{k}\cdot(\bar{r}_1-\bar{r}_0)} \bar{f}_0 \tag{2.17}$$

Thus for any arbitrary unit cell at a point P_n, the $\bar{f}$ vector can be expressed in terms of that of a unit cell at a global reference point P_0, as:

$$\bar{f}_n = e^{-i\bar{k}\cdot(\bar{r}_n-\bar{r}_0)} \bar{f}_0 \tag{2.18}$$

2.5.2 Array Factor

Let us consider a group of elements as shown in Figure 2-11 with unit cell dimensions d_x, d_y and d_z in the x,y and z directions respectively as already mentioned in Figure 2-1. The array factor due to an element with position indices [m,n,q] along [x,y,z] can be expressed using (2.18)as:

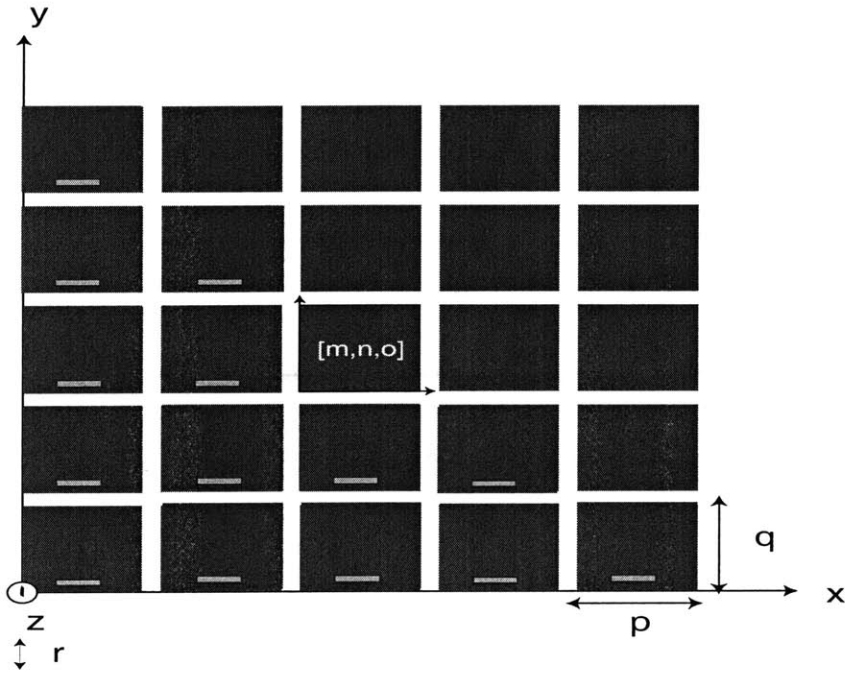

Figure 2-11: **A typical array of elements on the x-y plane**

$$\bar{f}_{mnq} = e^{-i\bar{k}\cdot\bar{r}_{mnq}+i\alpha_{mnq}}\bar{f}_0 \tag{2.19}$$

where, $\bar{f}_0$ is the $\bar{f}$ vector of the unit cell at the origin, and α_{mnq} is a progressive phase shift.

As an example, for a cubical array pattern with M, N and Q number of unit cells in the x,y and z directions respectively, the $\bar{f}$ due to all the elements is given as:

$$\bar{f} = \sum_{mnq} \bar{f}_{mnq} = \bar{f}_0 \sum_{mnq} e^{-i\bar{k}\cdot(\hat{x}(m-1)d_x+\hat{y}(n-1)d_y+\hat{z}(q-1)d_z)+i\alpha_{mnq}} \tag{2.20}$$

$$\Rightarrow \bar{f} = \bar{f}_0 \sum_{m=0}^{M-1} \sum_{n=0}^{N-1} \sum_{q=0}^{Q-1} e^{-ik(md_x sin(\theta)cos(\phi)+nd_y sin(\theta)sin(\phi)+qd_z cos(\theta))+i\alpha_{mnq}} \quad (2.21)$$

Therefore,

$$F = \sum_{m=0}^{M-1} \sum_{n=0}^{N-1} \sum_{q=0}^{Q-1} e^{-ik(md_x sin(\theta)cos(\phi)+nd_y sin(\theta)sin(\phi)+qd_z cos(\theta))+i\alpha_{mnq}} \quad (2.22)$$

is the array factor for the said cubical array pattern.

Thus, the array factor for any type of pattern can be obtain from (2.22) by defining the appropriate limits on [M,N,Q] and the corresponding summation scheme.

2.5.3 Validation

The Array factor formulation as determined above is validated here for known cases of antenna arrays. For all the cases presented here, all the array elements are on the x-y plane. And,the magnitude of the array factor, F, is plotted on the x-y plane, i.e $\theta = \pi/2$, as a function of the angle ϕ. Figure 2-12 shows the plot for a two element array (M=2,N=1,Q=1) along the x-axis with an inter-element distance ($d_x = d_y = d = \lambda/2$), and varying values of the progressive phase (α). Figure 2-13 shows the plot for a three element array (M=3,N=1,Q=1) along the x-axis with d= $\lambda/2$, and $\alpha = 0$, and that for a 2 x 2 element array (M=2,N=2,Q=1) on the x-y plane. And, Figure 2-14 shows the plots for N=5, $\alpha = \pi$ and d= $\lambda/2$ and d= $4\lambda/5$.

All these plots conform to those obtained using known analytical methods for determining array factors for antenna arrays [2]. Thus the formulation developed here can be treated as general and can be applied to any geometry by appropriate selection of the variables.

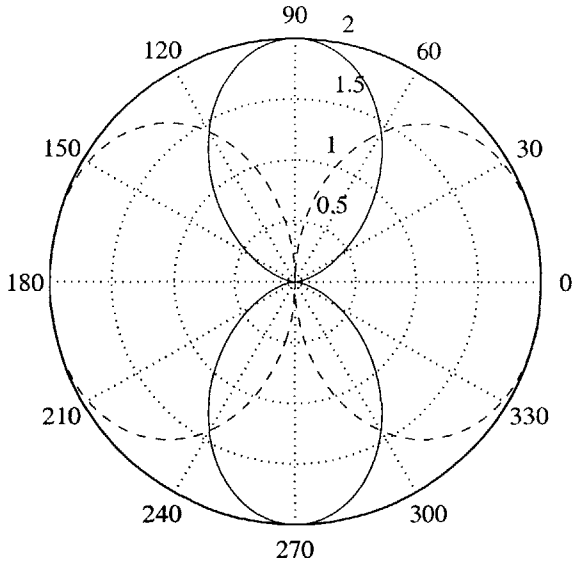

Figure 2-12: **Array Patterns for linear arrays obtained using (2.22). Solid Line: N=2, d=$\lambda/2$, Progressive phase (α)=0. Dashed Line: N=2, d=$\lambda/2$, $\alpha=\pi$**

2.6 Results

2.6.1 Determining the progressive phase

Inorder to determine the radiation pattern due to an S shaped SRR element, one needs to know the amplitude and phase of the current density each ring of the SRR. As seen in the previous sections, the current density on each ring can be expressed interms of the fourier modes and an anlytical expression can be thus be obtained. Using these current modes, the radiation pattern for each SRR can be obtained.

We have also developed a general formulation to obtain the array factor due to a composite made of such SRR elements. Using the radiation pattern due to a single ring and the array factor due to a composite structure, the radiation pattern due to the total structure can be determined. It is pertinent at this point to consider the inputs that are required to obtain this total radiation pattern. As is clear from the formulation, the only inputs that are required, other than the current distribution on a single SRR, are (1) information on the change of amplitude between subsequent

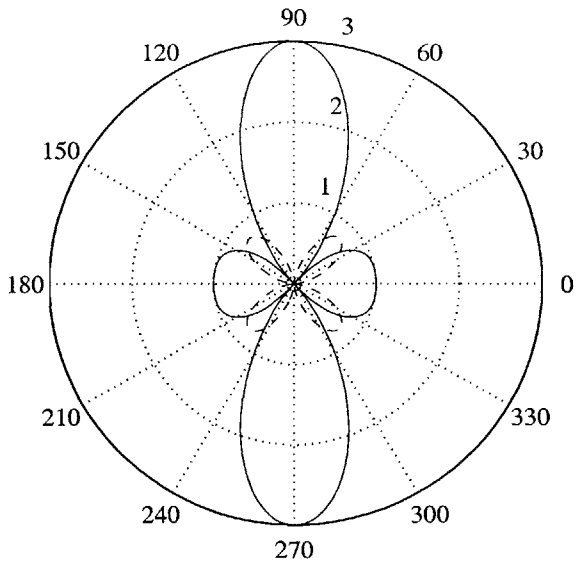

Figure 2-13: **Array Patterns for a linear arrays obtained using (2.22). Solid Line: N=3, d=λ/2, α=0. Dashed Line: N=2x2, d=λ/2, α=0**

elements, and (2) the progressive phase change between subsequent elements.

Inorder to determine these parameters, we study the case of an infinite slab consisting of such elements, simulated using HFSS ^{TM}. The set-up is similar to that of Figure (2-2), except that we now have three elements in the direction of propagation as opposed to one element in Figure (2-2). Having three elements facilitates us to study the amplitude and phase of the currents on each of the three SRRs in the direction of propagation. The infinite dimensions in the other directions are achieved using the PEC/PMC boundary conditions as shown in Figure (2-2).

Figures 2-15 to 2-17 show the amplitudes and phases of the surface current densities (J) on the front rings of each of the three SRRs, along with the total J. Each Figure has four plots showing (a) Magnitude of each component of J (Jx,Jz Mag) (b) Phase of each component of J (Jx,Jz Phase) (c) Total value of each component of J (Jx,Jz total), and (d) The resultant J obtained from the two components (J total), with respect to the normalized distance along the ring. In the last plot showing (J total), the actual values have kinks at the positions corresponding to the corners of the rings due to numerical problems in evaluating the currents at those points.

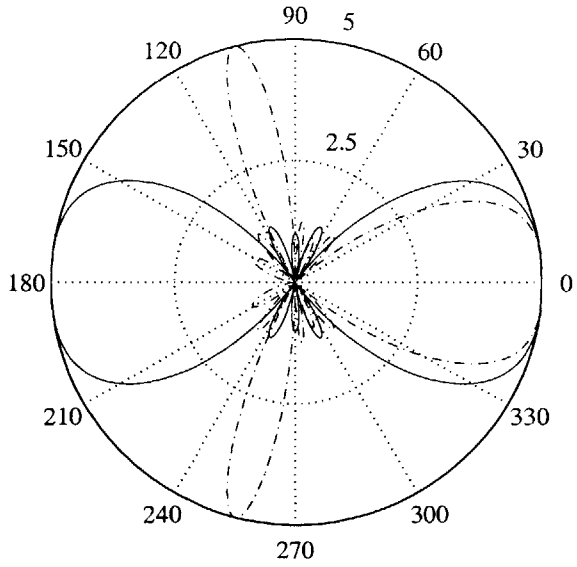

Figure 2-14: **Array Pattern for a linear arrays obtained using (2.22). Solid line: N=5, d=$\lambda/2$, $\alpha=\pi$. Dashed Line: N=5, d=$4\lambda/5$, $\alpha=\pi$**

These kinks have been smoothened using linear interpolation. The interpolated plot is shown along with the actual values. It is to be noted that each ring lies in the x-z plane, so that J has only x and z components.

It can be seen from (2-15) to (2-17) that the amplitudes of each component of (Jx,Jz Mag) are the same for each of the three rings. However, the phase of each component varies across the rings, causing a net variation in the total J. So, for an array of SRR elements along the propagation direction, the amplitude of J along each of the elements can be expected to be a constant function of the position, however there is a phase difference across the elements. It is thus imperative to examine the progressive phase increment/decrement between subsequent SRR elements.

Figure (2-18) shows the phase differences between adjacent elements of the three element setup. The figure consists of two parts showing (a) the phase difference between rings 1 and 2, δ_{21} and (b) the phase difference between rings 2 and 3, δ_{32}, as a funtion of the position along the rings. The plots show the phase differences between each component of J, i.e J_x and J_z. However, it is to be noted here that at a particular position along the ring, only the phase of that component of J is

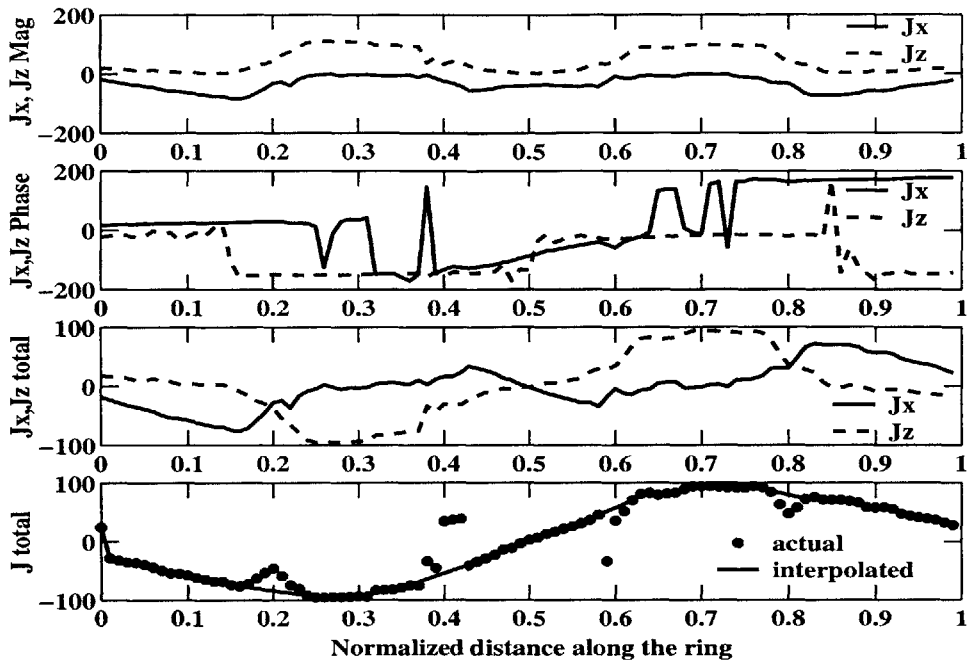

Figure 2-15: **Surface current density on the First ring in the propagation direction inside a waveguide**

relevant which has a dominant amplitude. Correspondingly, the value J_{21} and J_{32} show the relevant phase differences in each situation. It can be seen from both the plots that the phase differences between the first and the second rings is same as that between the second and third rings, at every position along the rings, and equals 125^o. Using the $e^{i(\omega t - \phi)}$ notation adopted in HFSS ^{TM} in speciying the phase of an Electromagnetic wave, this difference corresponds to a progressive phase increment of -125^o, i.e $\alpha = -125^o$.

This backward increment of progressive phase is one of the indications of an LH medium. Having obtained α, we can now use it in the array pattern formulation of a required composite struture, and determine the corresponding array factor. This array factor, in conjuction with the radiation pattern due to a single element will give us the radiation pattern due to the entire structure.

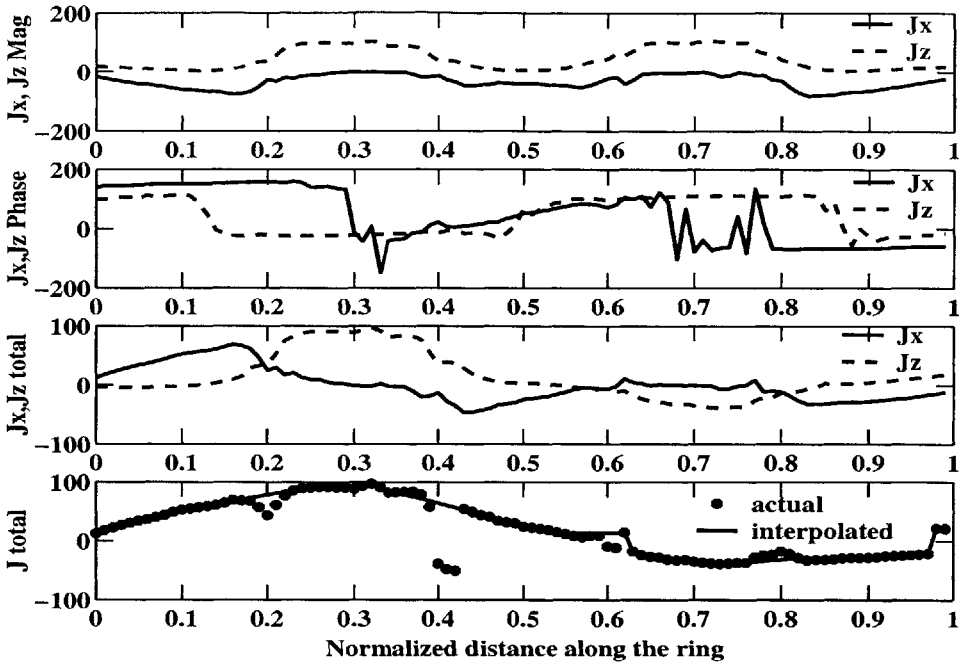

Figure 2-16: Surface current density on the Second ring in the propagation direction inside a waveguide

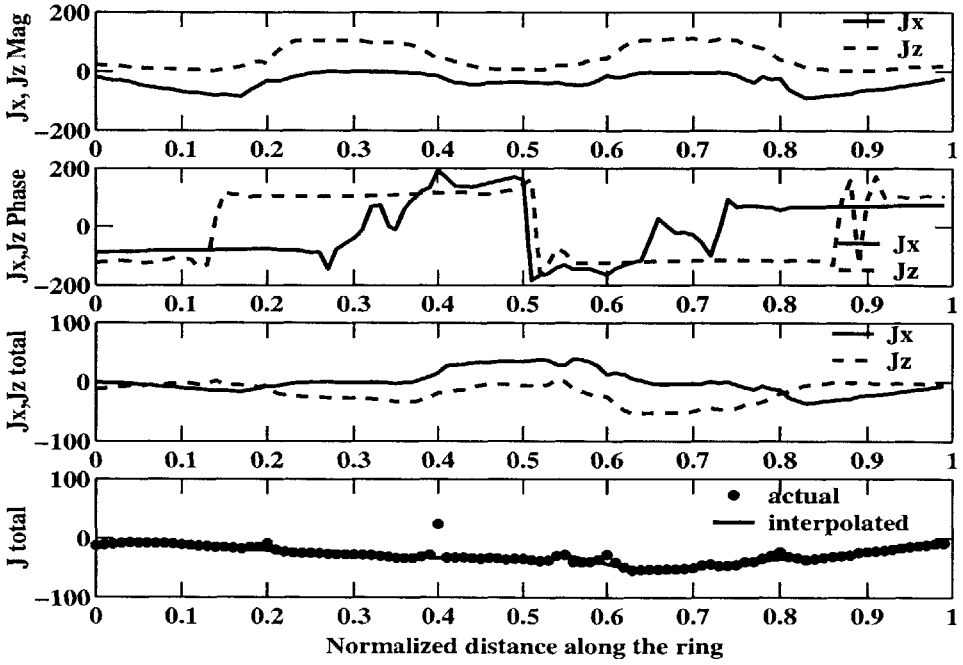

Figure 2-17: Surface current density on the Third ring in the propagation direction inside a waveguide

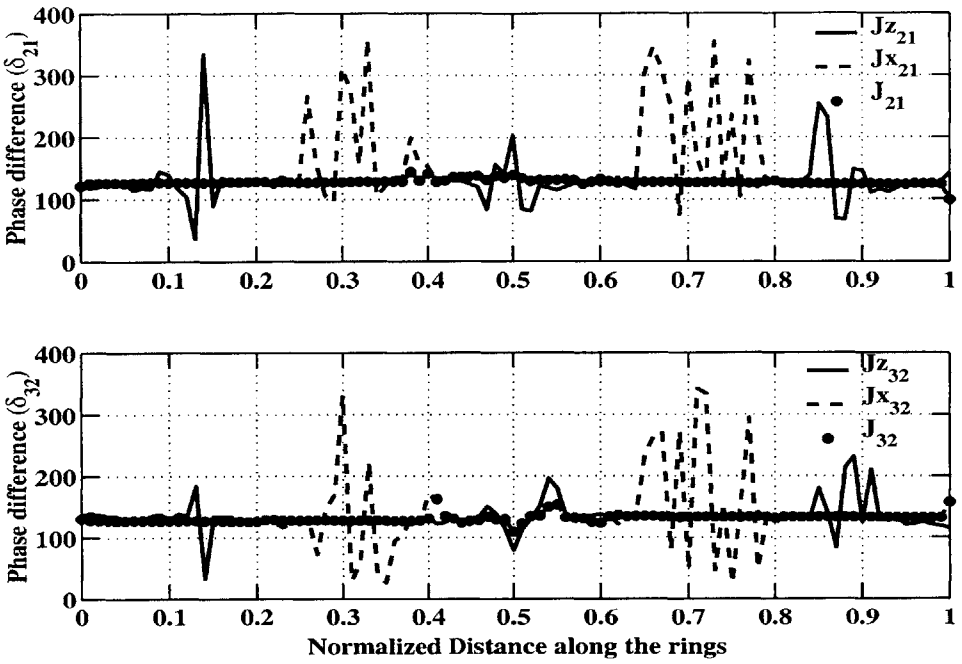

Figure 2-18: **Phase difference between adjacent rings**

2.6.2 Radiation Pattern for S-ring Prism

As seen in the previous sections, the vector current moment for a single SRR can be obtained using (2.11) and the corresponding radiation pattern can be obtained using (2.13). For an array of elements, the array factor can be obtained using (2.22). The total vector current moment for the array of elements can then be obtained using

$$\bar{f} = \bar{f}_o F$$

where, $\bar{f}_o$ is the vector current moment due to a single SRR and F is the array pattern of the array of elements.

The current formulation will now be used to determine the refracted radiation due to a prism of S-shaped SRRs. Figure 2-19 shows a typical set-up of the problem. A two-dimensional array of elements forming a prism on the x-y plane is shown. All the SRRs stand parallel to the x-z plane. The excitation is due to a plane wave propagating in the x-direction, with the $\bar{E}$ vector in the z direction and the $\bar{H}$ vector

in the y direction. The unit cell dimensions are kept the same, i.e, 4mm, 2.5mm and 5.4mm in the x,y and z directions.

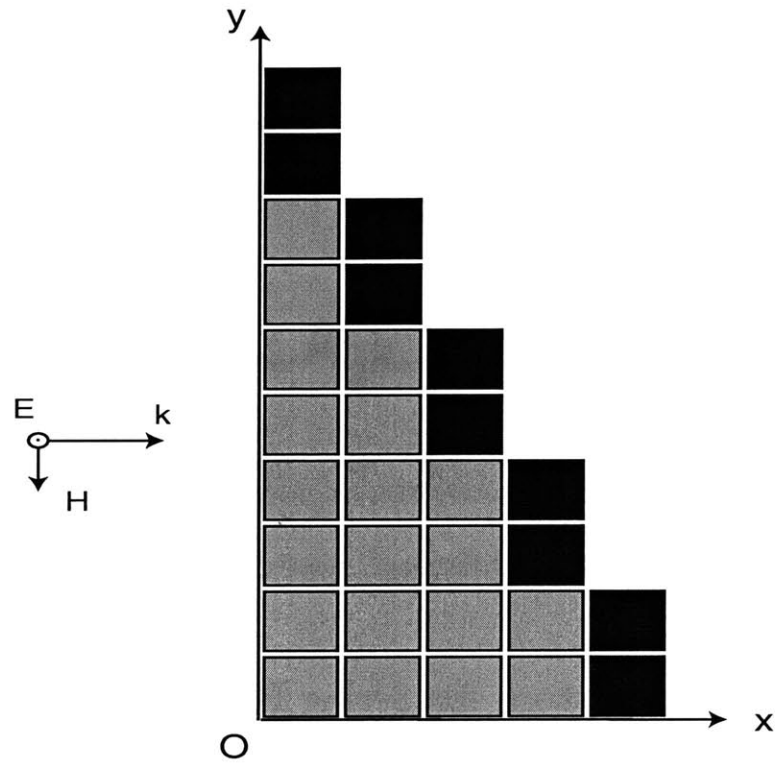

Figure 2-19: **A sample prism**

Two cases with prism angles (η) of 28^o and 39^o are considered. For the $\eta = 28^o$ case, there are 5 elements along the xaxis and 15 elements along the y axis, forming a 1:3 stagger ($\eta = tan^{-1}(\frac{4}{3\times2.5} = 28.07^o)$). For the $\eta = 39^o$ case, there are 5 elements along the xaxis and 10 elements along the y axis, forming a 1:2 stagger ($\eta = tan^{-1}(\frac{4}{2\times2.5} = 38.7^o)$).

A progressive phase (α) of -125^o is used, as determined from the previous section, between adjacent layers of elements along the x axis. And, only the edge elements of the prism are considered to be radiating. These elements are marked in the Figure 2-19. This choice of considering only the end elements is due to the fact that the radiation due to the previous elements is shielded by the successive ones leading to no contribution on the x-y plane in the far field that is of interest here. A detailed

study about this approach to obtain the radiation pattern is studied in [21]

The results from the two aforementioned cases are shown in Figures (2-20) and (2-21). As can be clearly observed both the figures indicate maximum radiation on that side of the normal which pertains to negative refraction. The normals in both the figures are indicated by the dotted lines and the prism-air slanted interface is indicated by a slanted solid line. It can be observed that the angle of refraction (θ_r) for $\eta = 28^o$ is 47^o, in the negative region. Using the Snell's law,

$$n_{prism} sin(\theta_i) = n_{air} sin(\theta_r)$$

where, n_{prism} is the effective refractive index of the SRR medium and n_{air} is the refractive index of free space, we have, n_{prism} = -1.55.

And, for the case with $\eta = 39^o$, it can be observed that $\theta_r = 66^o$, giving an effective refractive index of -1.45.

Thus, it can be seen that values of n obtained for both the cases described above approximately match with the n retrieved from the S-parameters (i.e n = -1.59). The apparently minor differences between the values can be attributed to the irregular edges of the prisms.

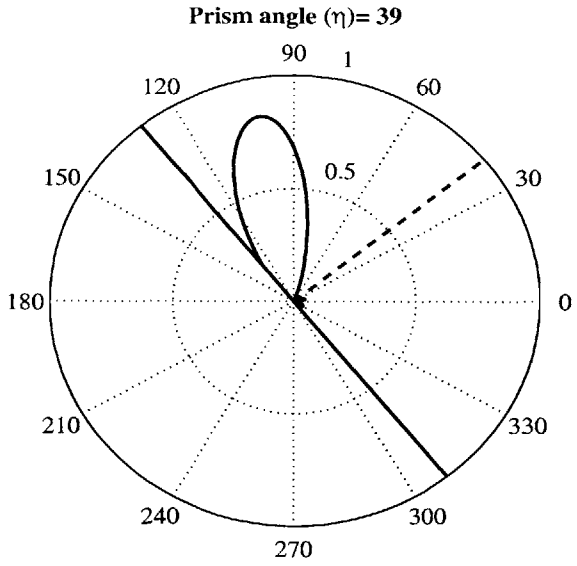

Figure 2-20: **Normalized Radiation due to prism with angle $\eta = 39^o$ The solid slanted line shows the prism edge, and the dashed line shows the normal**

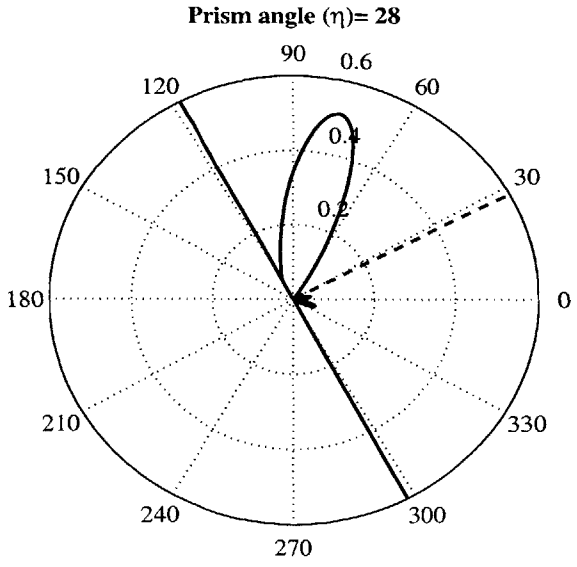

Figure 2-21: **Normalized Radiation due to prism with angle $\eta = 28^o$ The solid slanted line shows the prism edge, and the dashed line shows the normal**

Chapter 3

Polarizers using Metamaterials

3.1 Introduction

Metamaterials are materials having negative permittivity or permeability or both, being known as 'Left Handed Materials' in the latter case. Many applications of these materials have recently been proposed and thoroughly investigated. In the present work, we explore the polarizing capabilities of metamaterials having only a negative uniaxial permittivity tensor and an isotropic free-space permeability.

Polarizers are one of the most widely used components in optical applications. Traditionally, the most widely used polarizers are sheet polarizers which are essentially membranes of submicroscopic dichoric crystals. A dichoric crystal is an uniaxially anisotropic molecular assembly. An unpolarized wave entering such a medium is split up into linearly polarized ordinary and extraordinary waves [2]. Correspondingly, two types of polarizers are possible, O-type and E-type. O-type polarizers transmit ordinary waves, whereas E-type polarizers transmit extraordinary waves. Conventional sheet polarizers are O-type polarizers. A typical O-type polarizer has a complex permittivity along the optic axis with a large imaginary part. This leads to an attenuating extra-ordinary wave, while the ordinary wave is transmitted. Recently, E-type polarizers have also come into existence. These polarizers transmit the extraordinary waves while attenuating the ordinary waves.

The basic principle underlying the development of polarizers was first introduced by E. H. Land in the 1920s. With the recent advances in thin film manufacturing technologies, the thickness of the polarizers have been considerably reduced, to nanometers, and the coating techniques have developed greatly [13]. There has also been a significant increase in the durability of the dichroic sheets, owing to high performance requirements of applications like Liquid Crystal Displays. Nevertheless, polarizers still face some basic problems, like, leakage in crossed polarizers, heat due to attenuation, etc. In this chapter, the transmission of electromagnetic waves through crossed polarizers is studied and the leakages (Transmittances) in different types of polarizers are compared.

3.2 Uniaxial Media

All polarizers are essentially uniaxial media. In trying to study the polarizing capabilities of metamaterials, therefore, it is imperative to analyze the basic concepts of electromagnetic wave propagation through uniaxial media. This would enable us to develop formulations for any characteristic property of the media. Typically, for polarizers, two properties of interest are:

1. Wave propagation through crossed polarizers (also known as leakage), and

2. Fresnel reflection and transmission coefficients.

In the present section, we develop the tools to study these properties.

3.2.1 Wave Propagation through Uniaxial Media

Consider an uniaxial medium with permittivity ($\bar{\bar{\epsilon}}$) and impermittivity ($\bar{\bar{\kappa}}$) tensors, in the cartesian coordinate system, given by

$$\bar{\bar{\epsilon}} = \begin{bmatrix} \epsilon_e & 0 & 0 \\ 0 & \epsilon_o & 0 \\ 0 & 0 & \epsilon_o \end{bmatrix} \quad , \quad \bar{\bar{\kappa}} = \begin{bmatrix} \kappa_e & 0 & 0 \\ 0 & \kappa_o & 0 \\ 0 & 0 & \kappa_o \end{bmatrix} \tag{3.1}$$

where ϵ_o and ϵ_e are the ordinary and extraordinary permittivities, respectively. Let the isotropic permeability and impermeability be $\mu = \mu_o$ and $\nu = \frac{1}{\mu}$, where, μ_o is the permeability of free-space.

The wave vector in this system can be written as:

$$\bar{k}(\theta, \phi) = k(sin\theta cos\phi \hat{x} + sin\theta sin\phi \hat{y} + cos\theta \hat{z}) \tag{3.2}$$

The dispersion relation for this medium can be obtained by solving Maxwell's equations. In the present work, the kDB method [2] is used to solve Maxwell's equations in matrix form.

The kDB Method

The kDB method [2] establishes a coordinate system which simplifies solving the Maxwell's equations for homogeneous anistropic media. In this method, the cartesian coordinates $[\hat{x}\hat{y}\hat{z}]$ are transformed to the new coordinates $[\hat{e_1}\hat{e_2}\hat{e_3}]$, which comprise of the $\hat{k}$ vector and the $\hat{D} - \hat{B}$ plane. The $[\hat{e_1}\hat{e_2}\hat{e_3}]$ vectors form a set of orthogonal coordinate axes, with $\hat{e_3}$ lying along $\hat{k}$, and $\hat{e_1}$ and $\hat{e_2}$ lying in the $\hat{D} - \hat{B}$ plane. The advantage with this choice of orientation is that the $\hat{D}$ and $\hat{B}$ vectors in this system have only two components, thereby reducing the dimensions of Maxwell's equations in matrix form.

The new coordinate axes can be expressed in terms of the cartesian coordinates as:

$$\begin{aligned} \hat{e_3} &= \hat{k} = (sin\theta cos\phi\hat{x} + sin\theta sin\phi\hat{y} + cos\theta\hat{z}) \\ \hat{e_2} &= (cos\theta cos\phi\hat{x} + cos\theta sin\phi\hat{y} - sin\theta\hat{z}) \\ \hat{e_1} &= (sin\phi\hat{x} - cos\phi\hat{y}) \end{aligned} \tag{3.3}$$

With this choice of coordinates the transformation matrix for can be written as

$$\overline{\overline{T}} = \begin{bmatrix} sin\phi & -cos\phi & 0 \\ cos\theta cos\phi & cos\theta sin\phi & -sin\theta \\ sin\theta cos\phi & sin\theta sin\phi & cos\theta \end{bmatrix} \tag{3.4}$$

so that any vector $\overline{V}$ in the cartesian coordinates can be transformed into the new coordinates as:

$$\overline{V}' = \overline{\overline{T}} \cdot \overline{V} \tag{3.5}$$

and, any tensor $\overline{\overline{X}}$ can be transformed as:

$$\overline{\overline{X'}} = \overline{\overline{T}} \cdot \overline{\overline{X}} \cdot \overline{\overline{T}}^{-1} \tag{3.6}$$

Thus for any given media, the constitutive properties (permittivity and permeability) and the Electric and Magnetic fields can always be transformed to obtain Maxwell's equations in the kDB system.

Maxwell's equations in homogeneous media can thus be written as:

$$\begin{aligned} \overline{k} \times \overline{E'} &= \omega \overline{B'} \\ \overline{k} \times \overline{H'} &= -\omega \overline{D'} \\ \overline{k} \cdot \overline{B'} &= 0 \\ \overline{k} \cdot \overline{D'} &= 0 \end{aligned} \tag{3.7}$$

where, $\overline{k} = k\hat{e_3}$, and the primes indicate the vectors in the kDB system. The vectors $\overline{E'}, \overline{D'}, \overline{H'}$ and $\overline{B'}$ are related via the constitutive relations as:

$$\overline{E'} = \overline{\overline{\kappa'}} \cdot \overline{D'} + \overline{\overline{\chi'}} \cdot \overline{B'} \qquad \overline{H'} = \overline{\overline{\nu'}} \cdot \overline{B'} + \overline{\overline{\gamma'}} \cdot \overline{D'} \tag{3.8}$$

Substituing these relations in Maxwell's equations, we can rewrite the equations as :

$$\begin{bmatrix} \kappa'_{11} & \kappa'_{12} \\ \kappa'_{21} & \kappa'_{22} \end{bmatrix} \begin{bmatrix} D'_1 \\ D'_2 \end{bmatrix} = - \begin{bmatrix} \chi'_{11} & \chi'_{12} - u \\ \chi'_{21} + u & \chi'_{22} \end{bmatrix} \begin{bmatrix} B'_1 \\ B'_2 \end{bmatrix} \tag{3.9}$$

$$\begin{bmatrix} \nu'_{11} & \nu'_{12} \\ \nu'_{21} & \nu'_{22} \end{bmatrix} \begin{bmatrix} B'_1 \\ B'_2 \end{bmatrix} = - \begin{bmatrix} \gamma'_{11} & \gamma'_{12} + u \\ \gamma'_{21} - u & \gamma'_{22} \end{bmatrix} \begin{bmatrix} D'_1 \\ D'_2 \end{bmatrix} \tag{3.10}$$

where, $\omega/k = u$ is the phase velocity.

Thus by substituting the transformed elements of the $\overline{\overline{\kappa}}, \overline{\overline{\chi}}, \overline{\overline{\nu}}$ and $\overline{\overline{\gamma}}$ tensors, into the matrix equation and by eliminating D_1, D_2, B_1 and B_2, the dispersion relations can be obtained.

Dispersion relation for the uniaxial medium

Considering the $\overline{\overline{\kappa}}$ and $\overline{\overline{\nu}}$, tensors in eq.[1], and noting that $\overline{\overline{\chi}} = \overline{\overline{\gamma}} = 0$, we have:

$$\begin{bmatrix} \kappa'_{11} & \kappa'_{12} \\ \kappa'_{21} & \kappa'_{22} \end{bmatrix} \begin{bmatrix} D'_1 \\ D'_2 \end{bmatrix} = -\begin{bmatrix} 0 & -u \\ u & 0 \end{bmatrix} \begin{bmatrix} B'_1 \\ B'_2 \end{bmatrix} \tag{3.11}$$

$$\nu \begin{bmatrix} B'_1 \\ B'_2 \end{bmatrix} = -\begin{bmatrix} 0 & u \\ -u & 0 \end{bmatrix} \begin{bmatrix} D'_1 \\ D'_2 \end{bmatrix} \tag{3.12}$$

where, $\kappa'_{11} = \kappa_e sin^2\phi + \kappa cos^2\phi$, $\kappa'_{12} = \kappa'_{21} = (\kappa_e - \kappa)cos\theta sin\phi cos\phi$, and $\kappa'22 = (\kappa_e - \kappa)cos^2\theta cos^2\phi + \kappa$

Eliminating $\begin{bmatrix} B'_1 \\ B'_2 \end{bmatrix}$, from the two equations we have,

$$\begin{bmatrix} \nu\kappa'_{11} - u^2 & \nu\kappa'_{12} \\ \nu\kappa'_{21} & \nu\kappa'_{22} - u^2 \end{bmatrix} \begin{bmatrix} D'_1 \\ D'_2 \end{bmatrix} = 0 \tag{3.13}$$

Setting the determinant of the 2×2 matrix to zero, and noting that $u = \omega/k$, we obtain the dispersion relations for the ordinary and extraordinary wave vectors as:

$$\omega^2 = \frac{k^2}{\mu\epsilon_o} \tag{3.14}$$

$$\omega^2 = \frac{k^2}{\mu}[sin^2\theta cos^2\phi(\frac{1}{\epsilon_o} - \frac{1}{\epsilon_e}) + \frac{1}{\epsilon_e}] \tag{3.15}$$

3.2.2 Leakage in crossed polarizers

A wave entering an uniaxial medium seperates into two components: an ordinary wave and an extraordinary wave. The ordinary wave has its electric displacement vector, $\overline{D_o}$, and hence its polarization, perpendicular to the plane containing the optic axis, $\hat{c}$, and its wave vector, $\hat{k_o}$. On the other hand, the extraordinary wave has its electric displacement, $\overline{D_e}$, in the place containing $\hat{c}$ and its wave vector, $\hat{k_e}$. A complete study of wave propagation though a pair of crossed polarizers involves the determination of two factors:

a. Angles of transmission through both the polarizers for the ordinary and extraordinary waves,

b. Transmittances (or leakage) of the ordinary and extraordinary waves through a pair of crossed polarizers.

Let us consider two polarizers with their optic axes along the $\hat{x}$ and $\hat{y}$ axes respectively, in the cartesian coordinate system. Let $[\theta_i, \phi]$ be the angle of incidence of the incident wave moving from free-space into the medium.

The effective refractive indices for the ordinary and extraordinary waves ($n(o)$ and $n(e)$) for a single polarizer can be obtained from the dispersion relations as:

$$n(o) = n_o \tag{3.16}$$

$$\frac{1}{n(e)^2} = sin^2\theta cos^2\phi(\frac{1}{n_o^2} - \frac{1}{n_e^2}) + \frac{1}{n_e^2} \tag{3.17}$$

where, $n_o = \sqrt{\epsilon_o \mu_o / c^2}$ and $n_e = \sqrt{\epsilon_e \mu_o / c^2}$, where c is the speed of light in free-space.

Angles of transmission

Propagation of Ordinary Wave

By phase matching across the free-space - Slab boundary, for the first polarizer, we have:

$$n_i sin\theta_i = n_1 sin\theta_1 \tag{3.18}$$

where, n_1 and θ_1 are the refractive index of the first polarizer and the angle of transmission, respectively, for ordinary wave propagation.

Since $n_i = 1$ (free-space) and $n_1 = n_o$, we have:

$$sin\theta_1 = \frac{sin\theta_i}{n_o} \tag{3.19}$$

For the second polarizer, $n_1 sin\theta_1 = n_2 sin\theta_2$, where, n_2 and θ_2 are the refractive index of the second polarizer and the angle of transmission, respectively, for ordinary wave propagation.

Since $n_1 = n_2 = n_o$, we have:

$sin\theta_1 = sin\theta_2$ or $\theta_1 = \theta_2 = \theta_o$

Therefore the direction of the propagation vector of the ordinary wave remains constant through both polarizers, and is specified by:

$$sin\theta_o = \frac{sin\theta_i}{n_o} \tag{3.20}$$

Propagation of Extraordinary Wave:

The effective extraordinary refractive index for the first polarizer (with $\hat{c} = \hat{x}$) is given as:

$$\frac{1}{n(e)^2} = sin^2\theta cos^2\phi(\frac{1}{n_o^2} - \frac{1}{n_e^2}) + \frac{1}{n_e^2} \tag{3.21}$$

By phase matching the incident wave with the extraordinary wave, we have:

$$n_i sin\theta_i = n(e) sin\theta_e \Rightarrow \frac{1}{n(e)^2} = \frac{sin^2\theta_e}{sin^2\theta_i} \tag{3.22}$$

where, θ_e, is the angle of propagation of the extraordinary wave in the medium. By substituting for $\frac{1}{n(e)^2}$ from (21) and solving for $sin\theta_e$, we have:

$$sin\theta_{e1} = \frac{n_o sin\theta_i}{\sqrt{[n_o^2 n_e^2 - sin\theta_i^2 cos\phi^2(n_e^2 - n_o^2)]}} \tag{3.23}$$

For the second polarizer (with $\hat{c} = \hat{y}$), the effective extraordinary refractive index is obtained as:

$$\frac{1}{n(e)^2} = sin^2\theta sin^2\phi(\frac{1}{n_o^2} - \frac{1}{n_e^2}) + \frac{1}{n_e^2} \tag{3.24}$$

Proceeding similarily as in the previous case, the angle of propagation in this case can be obtained as:

$$sin\theta_{e2} = \frac{n_o sin\theta_i}{\sqrt{[n_o^2 n_e^2 - sin\theta_i^2 sin\phi^2(n_e^2 - n_o^2)]}} \tag{3.25}$$

Thus for any given incidence, $[\theta_i, \phi]$, we can now obtain the angles of propagation of the ordinary and extraordinary waves in both the polarizers. Therefore, the ordinary and extraordinary propagation vectors, $\hat{k_o}$ and $\hat{k_e}$ are determined for both the polarizers.

Transmittance (leakage) through crossed polarizers

Leakage is defined as the amount of unpolarized light passing through the two polarizers. It is determined by the projection of the ordinary and extraordinary wave vectors of the first polarizer along those of the second polarizer. Correspondingly, there are two components of leakage: one due to the ordinary waves and another due to the extraordinary waves.

Leakage due to ordinary waves

The propagation vector of an ordinary wave can be written as:

$$\overline{k_o} = k_o(sin\theta_o cos\phi\hat{x} + sin\theta_o sin\phi\hat{y} + cos\theta_o\hat{z}) \tag{3.26}$$

Since the electric displacement, $\overline{D_o}$, is perpendicular to the plane containing the optic axis, $\hat{c}$, and its wave vector, $\hat{k_o}$, a unit vector along it can be expressed as:

$$\hat{o} = \frac{\hat{k_o} \times \hat{c}}{|\hat{k_o} \times \hat{c}|} \tag{3.27}$$

Therefore, the $\hat{o}$ vectors for the first and second polarizers can be obtained as:

$$\hat{o_1} = \frac{\hat{k_o} \times \hat{x}}{|\hat{k_o} \times \hat{x}|} = \frac{\hat{y}cos\theta_o - \hat{z}sin\theta_o sin\phi}{\sqrt{1 - sin^2\theta_o cos^2\phi}} \tag{3.28}$$

$$\hat{o_2} = \frac{\hat{k_o} \times \hat{y}}{|\hat{k_o} \times \hat{y}|} = \frac{-\hat{x}cos\theta_o + \hat{z}sin\theta_o cos\phi}{\sqrt{1 - sin^2\theta_o sin^2\phi}} \tag{3.29}$$

From these vectors, the leakage of ordinary waves through the pair of crossed polarizers is obtained as:

$$T_o = \frac{1}{2}|\hat{o_1} \cdot \hat{o_2}|^2 \tag{3.30}$$

Leakage due to extraordinary waves

The propagation vector of an extraordinary wave can be written as:

$$\overline{k_e} = k_e(sin\theta_e cos\phi\hat{x} + sin\theta_e sin\phi\hat{y} + cos\theta_e\hat{z}) \tag{3.31}$$

Since the electric displacement, $\overline{D_e}$, lies in the place containing $\hat{c}$ and its wave vector, $\hat{k_e}$, the unit vector along it can be expressed as:

$$\hat{e} = \frac{\hat{k}_e \times \hat{o}}{|\hat{k}_e \times \hat{o}|} \tag{3.32}$$

Therefore, as for the ordinary case, the $\hat{e}$ vector for the two polarizers can be obtained as:

$$\hat{e_1} = \frac{\hat{k_{e1}} \times \hat{o}_1}{|\hat{k}_{e1} \times \hat{o}_1|} \tag{3.33}$$

and

$$\hat{e_2} = \frac{\hat{k}_{e2} \times \hat{o}_2}{|\hat{k}_{e2} \times \hat{o}_2|} \tag{3.34}$$

and the leakage of extraordinary waves can be obtained as:

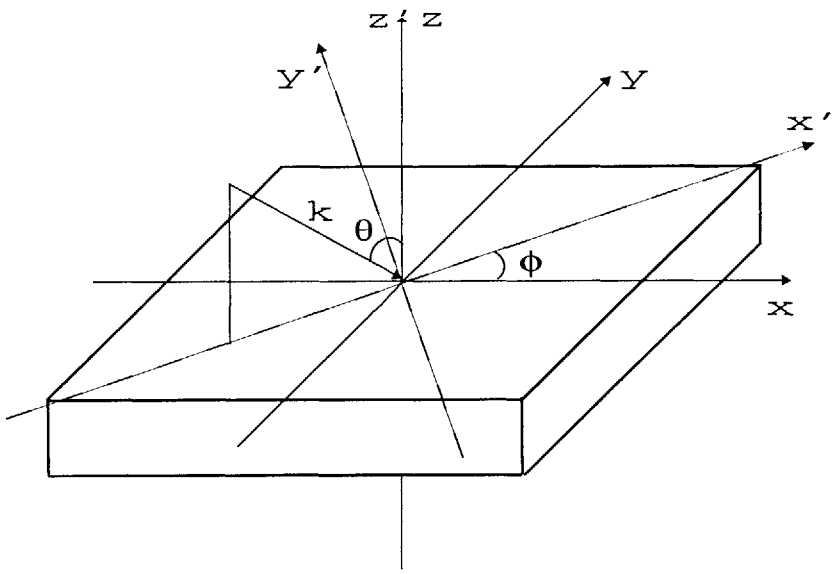

Figure 3-1: **A Uniaxial slab with optic axis along the x-axis**

$$T_e = \frac{1}{2}|\hat{e_1} \cdot \hat{e_2}|^2 \tag{3.35}$$

Thus we have constructed the general formalism to obtain the leakages through pairs of crossed ordinary and extraordinary polarizers.

3.3 Fresnel Coefficients of a Uniaxial Slab

3.3.1 Transformation of the Permittivity Tensor

Consider a slab with uniaxial permittivity and impermittivity tensors given by

$$\bar{\bar{\epsilon}} = \begin{bmatrix} \epsilon_e & 0 & 0 \\ 0 & \epsilon_o & 0 \\ 0 & 0 & \epsilon_o \end{bmatrix} \quad ; \quad \bar{\bar{\kappa}} = \begin{bmatrix} \kappa_e & 0 & 0 \\ 0 & \kappa_o & 0 \\ 0 & 0 & \kappa_o \end{bmatrix} \tag{3.36}$$

and the isotropic permeability and impermeability give by, $\mu = \mu_o$ and $\nu = \frac{1}{\mu}$.

As can be seen from the tensors,the optic axis is chosen to be along the x axis.

This is because, the slab is on the x-y plane and the z axis is along the normal, as shown in Figure 3-1. There is no loss of generality in chosing the optic axis along the x-axis, as the slab can always be rotated about the z-axis to orient the optic axis along the coordinate axis of interest, on the x-y plane. Figure 3-1 also shows an incident wave, $\overline{k}(\theta, \phi)$, given by

$$\overline{k}(\theta, \phi) = k(sin\theta cos\phi \hat{x} + sin\theta sin\phi \hat{y} + cos\theta \hat{z}) \tag{3.37}$$

where, θ is the angle with the normal,$\hat{z}$, and ϕ is the angle between $\hat{x}$ and the projection of the wave vector on the x-y plane. The dispersion relation for the general case of any incidence can be solved using Maxwell's equations. However, in order to simplify the analysis of the TE and TM propagation, the coordinate axes can be transformed so as to keep the $\overline{k}$ vector in the x'-z' plane of the transformed coordinate system.The transformation tensor can therefore be expressed as:

$$\overline{\overline{T}} = \begin{bmatrix} cos(\phi) & sin(\phi) & 0 \\ -sin(\phi) & cos(\phi) & 0 \\ 0 & 0 & 1 \end{bmatrix} \tag{3.38}$$

so that

$$\overline{k'} = \overline{\overline{T}} \cdot \overline{k} \tag{3.39}$$

where, $\overline{k'}$ is the transformed wave vector. The ϕ now represents the angle by which the axes are transformed. And the wave vector now lies in the x'-z' plane of the transformed co-ordinate system shown in 3-1. The transformed permittivity tensor in the new coordinate axes $[\hat{x}'\hat{y}'\hat{z}']$ is obtained as:

$$\overline{\overline{\epsilon'}} = \overline{\overline{T}} \cdot \overline{\overline{\epsilon}} \cdot \overline{\overline{T^{-1}}} = \begin{bmatrix} \epsilon_e cos^2\phi + \epsilon_o sin^2\phi & (\epsilon_o - \epsilon_e) sin\phi cos\phi & 0 \\ (\epsilon_o - \epsilon_e) sin\phi cos\phi & \epsilon_e sin^2\phi + \epsilon_o cos^2\phi & 0 \\ 0 & 0 & \epsilon_o \end{bmatrix} \tag{3.40}$$

The dispersion relation for this tensor can be obtained by the kDB method men-

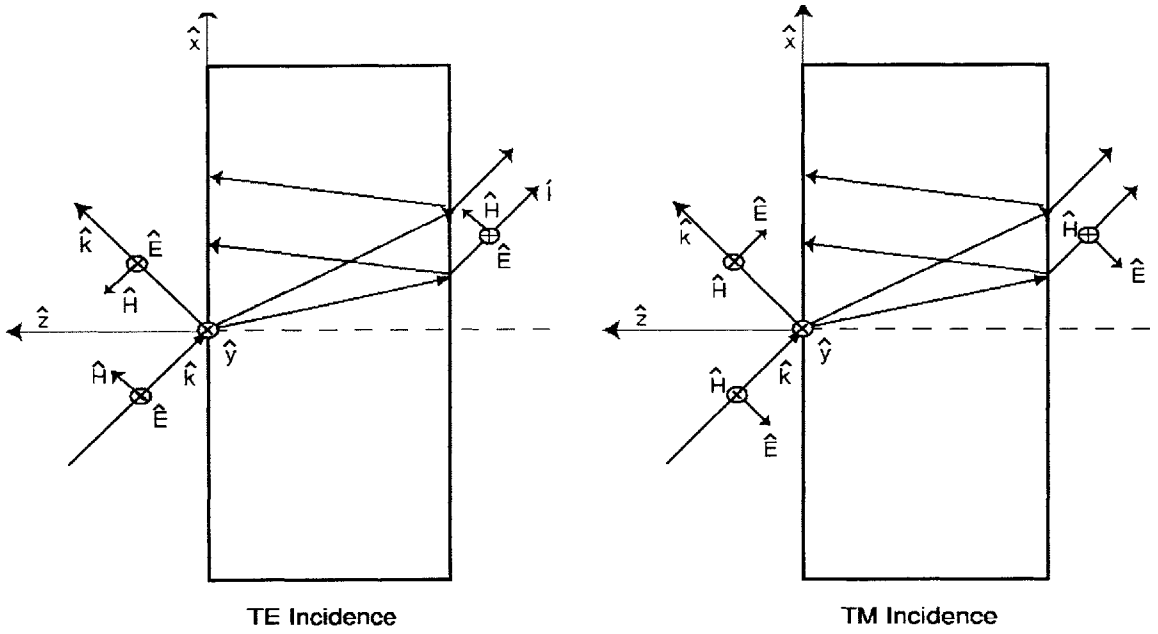

Figure 3-2: **Schematic diagrams of TE and TM Incidence**

tioned earlier. And by phase matching the angles of transmission for the ordinary and extraordinary propagation vectors can be obtained. We have obtained these angles numerically for all angles of incidence. It should be noted that in the new coordinated system $\overline{k} = k_x\hat{x}' + k_z\hat{z}'$. We shall drop the primes hence forth and work only in the new coordinate system. We can now resolve the Electric and Magnetic fields into TE and TM components to obtain the Fresnel's Coefficients.

3.3.2 TE Incidence

A shematic diagram of TE incidence is shown in Figure 3-2. For normal incidence, it is well-known that a TE incidence gives rise to reflected and transmitted fields with only TE components. However, as has been illustrated in the figure, a non-normal TE incidence leads to the reflected and transmitted fields with both TE and TM components. This should be introduced in the formulation for fields in the three regions. As is shown in the figure, Region 0, air, is the region of incidence and reflection, Region 2 is the uniaxial slab, and Region 3, air, is the region of transmission.

Region 0

The electric field $\overrightarrow{E_0}$ in this region can be expressed as:

$$\overrightarrow{E_0} = E_0[(R\hat{y} + \frac{t_1}{k_0}(k_z\hat{x} - k_x\hat{z}))e^{ik_z z} + \hat{y}e^{-ik_z z}]e^{ik_x x} \tag{3.41}$$

where, the subscripts o and e refer to the ordinary and extraordinary components, respectively, of the field and wave vectors.

Using Maxwell's equations, the components of the corresponding Magnetic fields can be obtained as:

$$\begin{aligned}
H_{0x} &= -\frac{1}{i\omega\mu}\frac{\partial E_{0y}}{\partial z} = -\frac{E_0 k_z}{\omega\mu}(Re^{ik_z z} - e^{-ik_z z})e^{ik_x x} \\
H_{0z} &= \frac{1}{i\omega\mu}\frac{\partial E_{0y}}{\partial x} = \frac{E_0 k_x}{\omega\mu}(Re^{ik_z z} + e^{-ik_z z})e^{ik_x x} \\
H_{0y} &= \frac{1}{i\omega\mu}(\frac{\partial E_{0x}}{\partial z} - \frac{\partial E_{0z}}{\partial x}) = \frac{E_0 t_1}{k_0\omega\mu}(k_z^2 + k_x^2)e^{ik_z z}e^{ik_x x} = \frac{E_0 t_1 k_0}{\omega\mu}e^{ik_z z}e^{ik_x x}
\end{aligned} \tag{3.42}$$

Region 2

The Electric field in region 2 can similarily be expressed as :

$$\overrightarrow{E_2} = E_o[T\hat{(y)} + \frac{t_2}{k_o}(-k_z\hat{x} - k_x\hat{z})]e^{-ik_z z}e^{ik_x x} \tag{3.43}$$

Therefore, the rectangular components of the Electric field in region 2 are:

$$\begin{aligned}
E_{2x} &= -\frac{E_o t_2}{k_o}(k_z e^{-ik_z z}e^{ik_x x}) \\
E_{2y} &= E_o T e^{-ik_z z}e^{ik_x x} \\
E_{2z} &= -\frac{E_o t_2}{k_o}k_x e^{-ik_z z}e^{ik_x x}
\end{aligned} \tag{3.44}$$

The components of the corresponding Magnetic fields in region 2 are obtained as:

$$\begin{aligned} H_{2x} &= -\frac{1}{i\omega\mu}\frac{\partial E_{2y}}{\partial z} = \frac{k_z E_o T}{\omega\mu} e^{-ik_z z} e^{ik_x x} \\ H_{2z} &= \frac{1}{i\omega\mu}\frac{\partial E_{2y}}{\partial x} = \frac{k_x E_o T}{\omega\mu} e^{-ik_z z} e^{ik_x x} \\ H_{2y} &= \frac{1}{i\omega\mu}(\frac{\partial E_{2x}}{\partial z} - \frac{\partial E_{2z}}{\partial x}) = \frac{E_o t_2}{k_o \omega\mu}(k_z^2 + k_x^2) e^{-ik_z z} e^{ik_x x} = \frac{k_o E_o t_2}{\omega\mu} e^{-ik_z z} e^{ik_x x} \end{aligned} \tag{3.45}$$

Region 1

The rectangular components of the Electric field in region I are:

$$\begin{aligned} E_{Ix} &= (A_1 o_{1x} e^{-ik_{oz}z} + B_1 e_{1x} e^{-ik_{ez}z} + A_2 o_{2x} e^{ik_{oz}z} + B_2 e_{2x} e^{ik_{ez}z}) e^{ik_x x} \\ E_{Iy} &= (A_1 o_{1y} e^{-ik_{oz}z} + B_1 e_{1y} e^{-ik_{ez}z} + A_2 o_{2y} e^{ik_{oz}z} + B_2 e_{2y} e^{ik_{ez}z}) e^{ik_x x} \\ E_{Iz} &= (A_1 o_{1z} e^{-ik_{oz}z} + B_1 e_{1z} e^{-ik_{ez}z} + A_2 o_{2z} e^{ik_{oz}z} + B_2 e_{2z} e^{ik_{ez}z}) e^{ik_x x} \end{aligned} \tag{3.46}$$

The components of the corresponding Magnetic fields in region I are similarily obtained from maxwell equations as for regions 0 and 2.

Boundary Conditions

Applying boundary conditions on the fields in the three regions we have:

At x=0, z=0:

$$E_{0x} = E_{Ix}, E_{0y} = E_{Iy}, H_{0x} = H_{Ix}, H_{0y} = H_{Iy} \tag{3.47}$$

At x=0, z=d:

$$E_{2x} = E_{Ix}, E_{2y} = E_{Iy}, H_{2x} = H_{Ix}, H_2 y = H_{Iy} \tag{3.48}$$

The system of linear equations are obtained as:

$A_1 o_{1x} + B_1 e_{1x} + A_2 o_{2x} + B_2 e_{2x} - t_1 \frac{E_o k_z}{k_o} = 0$

$$A_1 o_{1y} + B_1 e_{1y} + A_2 o_{2y} + B_2 e_{2y} - RE_o = E_o$$

$$A_1 o_{1y} k_{oz} + B_1 e_{1y} k_{ez} - A_2 o_{2y} k_{oz} - B_2 e_{2y} k_{ez} + RE_o k_z = E_o k_z$$

$$A_1(o_{1x}k_{oz} + o_{1z}k_x) + B_1(e_{1x}k_{ez} + e_{1z}k_x) + A_2(o_{2z}k_x - o_{2x}k_{oz}) + B_2(e_{2z}k_x - e_{2x}k_{ez}) + t_1 E_o k_o = 0$$

$$(A_1 o_{1x} e^{-ik_{oz}d} + B_1 e_{1x} e^{-ik_{ez}d} + A_2 o_{2x} e^{ik_{oz}d} + B_2 e_{2x} e^{ik_{ez}d}) + t_2 \frac{E_o k_z}{k_o} e^{-ik_z d} = 0$$

$$(A_1 o_{1y} e^{-ik_{oz}d} + B_1 e_{1y} e^{-ik_{ez}d} + A_2 o_{2y} e^{ik_{oz}d} + B_2 e_{2y} e^{ik_{ez}d}) - TE_o e^{-ik_z d} = 0$$

$$A_1 o_{1y} k_{oz} e^{-ik_{oz}d} + B_1 e_{1y} k_{ez} e^{-ik_{ez}d} - A_2 o_{2y} k_{oz} e^{ik_{oz}d} - B_2 e_{2y} k_{ez} e^{ik_{ez}d} - Tk_z E_o e^{-ikzd} = 0$$

$$A_1(o_{1x}k_{oz} + o_{1z}k_x)e^{-ik_{oz}d} + B_1(e_{1x}k_{ez} + e_{1z}k_x)e^{-ik_{ez}d} + A_2(o_{2z}k_x - o_{2x}k_{oz})e^{ik_{oz}d} + B_2(e_{2z}k_x - e_{2x}k_{ez})e^{ik_{ez}d} + t_2 k_o E_o e^{-ik_z d} = 0$$

where o_{1x}, o_{1y} and o_{1z} are the components of the Electric field of the ordinary wave in the x,y and z directions, respectively, in Region I, and so on. Solving these, we obtain the reflection and transmission coefficients (Fresnel coefficients) of the slab for TE incidence, as shown in Figure 3-5, for $\phi = 45^o$. Figure 3-6 shows the validation of the formulation for a uniaxial slab for $\phi = 0$

Figures 3-4 and 3-3 show the validation of the formulation for the cases where the slab is constituted of free space and isotropic isotropic material respectively.

Figure 3-6 shows the validation of the formulation for a uniaxial slab for $\phi = 0$

3.3.3 TM Incidence

Similarily as in the case of Electric fields for TE incidence, the Magnetic fields inthe three regions for TM incidence can be obtained as:

Region 0

$$\overline{H_0} = H_o[(R\hat{y} + \frac{t_1}{k_o}(-k_z\hat{x} + k_x\hat{z}))e^{ik_z z} + \hat{y}e^{-ik_z z}]e^{ik_x x} \tag{3.49}$$

Region I

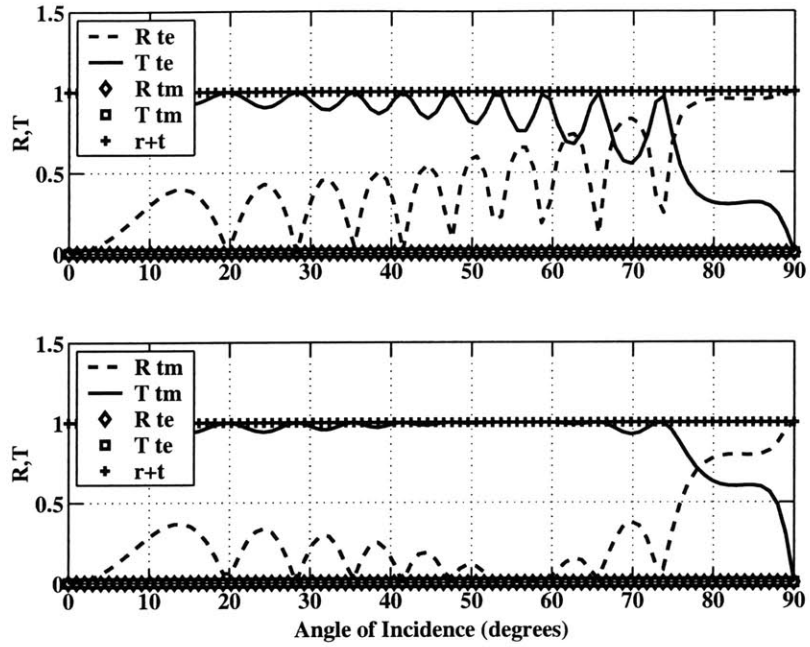

Figure 3-3: **Fresnel coefficients for an isotropic slab** ($n_0 = n_e = 1.5, \phi = 50^o$)

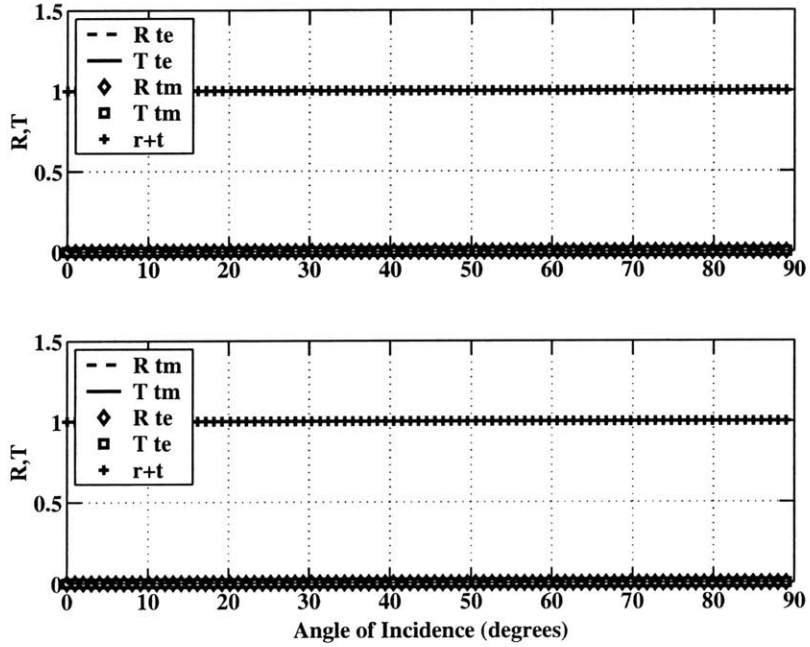

Figure 3-4: **Fresnel coefficients for free-space**($n_0 = n_e = 1, \phi = 50^o$)

$$H_{Ix} = (A_1 ho_{1x} e^{-ik_{oz}z} + B_1 he_{1x} e^{-ik_{ez}z} + A_2 ho_{2x} e^{ik_{oz}z} + B_2 he_{2x} e^{ik_{ez}z}) e^{ik_x x}$$
$$H_{Iy} = (A_1 ho_{1y} e^{-ik_{oz}z} + B_1 he_{1y} e^{-ik_{ez}z} + A_2 ho_{2y} e^{ik_{oz}z} + B_2 he_{2y} e^{ik_{ez}z}) e^{ik_x x} \quad (3.50)$$
$$H_{Iz} = (A_1 ho_{1z} e^{-ik_{oz}z} + B_1 he_{1z} e^{-ik_{ez}z} + A_2 ho_{2z} e^{ik_{oz}z} + B_2 he_{2z} e^{ik_{ez}z}) e^{ik_x x}$$

where, ho_{1x}, ho_{1x} and ho_{1x} are the magnetic analogues of o_{1x}, o_{1y} and o_{1z}, respectively, and so on.

Region 2

$$\overline{H_2} = H_o[T\hat{(y)} + \frac{t_2}{k_o}(k_z\hat{x} + k_x\hat{z})]e^{-ik_z z} e^{ik_x x} \quad (3.51)$$

Obtaining the Electric fields in the three regions and applying the boundary conditions give :

$$A_1 ho_{1x} + B_1 he_{1x} + A_2 ho_{2x} + B_2 he_{2x} + t_1 \frac{H_o k_z}{k_o} = 0$$

$$A_1 ho_{1y} + B_1 he_{1y} + A_2 ho_{2y} + B_2 he_{2y} - RH_o = H_o$$

$$A_1 a_{1x} + B_1 b_{1x} + A_2 a_{2x} + B_2 b_{2x} - R\frac{H_o k_z}{\epsilon_o} = -\frac{H_o k_z}{\epsilon_o}$$

$$A_1 a_{1y} + B_1 b_{1y} + A_2 a_{2y} + B_2 b_{2y} - T\frac{H_o k}{\epsilon_o} = 0$$

$$A_1 ho_{1x} e^{-ik_{oz}d} + B_1 he_{1x} e^{-ik_{ez}d} + A_2 ho_{2x} e^{ik_{oz}d} + B_2 he_{2x} e^{ik_{ez}d} - t_2 \frac{H_o k_z}{k} e^{-ik_z d} = 0$$

$$A_1 ho_{1y} e^{-ik_{oz}d} + B_1 he_{1y} e^{-ik_{ez}d} + A_2 ho_{2y} e^{ik_{oz}d} + B_2 he_{2y} e^{ik_{ez}d} - TH_o e^{-ik_z d} = 0$$

$$A_1 a_{1x} e^{-ik_{oz}d} + B_1 b_{1x} e^{-ik_{ez}d} + A_2 a_{2x} e^{ik_{oz}d} + B_2 b_{2x} e^{ikezd} + T\frac{H_o k_z}{\epsilon_o} e^{-ik_z d} = 0$$

$$A_1 a_{1y} e^{-ik_{oz}d} + B_1 b_{1y} e^{-ik_{ez}d} + A_2 a_{2y} e^{ik_{oz}d} + B_2 b_{2y} e^{ikezd} - t_2 \frac{H_o k}{\epsilon_o} e^{-ik_z d} = 0$$

where,

$$a_{1x} = (-\kappa_{11} ho_{1y} k_{oz} + \kappa_{12}(ho_{1x} k_{oz} + ho_{1z} k_x) - \kappa_{13} k_x ho_{1y})$$
$$b_{1x} = (-\kappa_{11} he_{1y} k_{ez} + \kappa_{12}(he_{1x} k_{ez} + he_{1z} k_x) - \kappa_{13} k_x he_{1y})$$
$$a_{2x} = (\kappa_{11} ho_{2y} k_{oz} + \kappa_{12}(ho_{2z} k_x - ho_{2x} k_{oz}) - \kappa_{13} k_x ho_{2y})$$

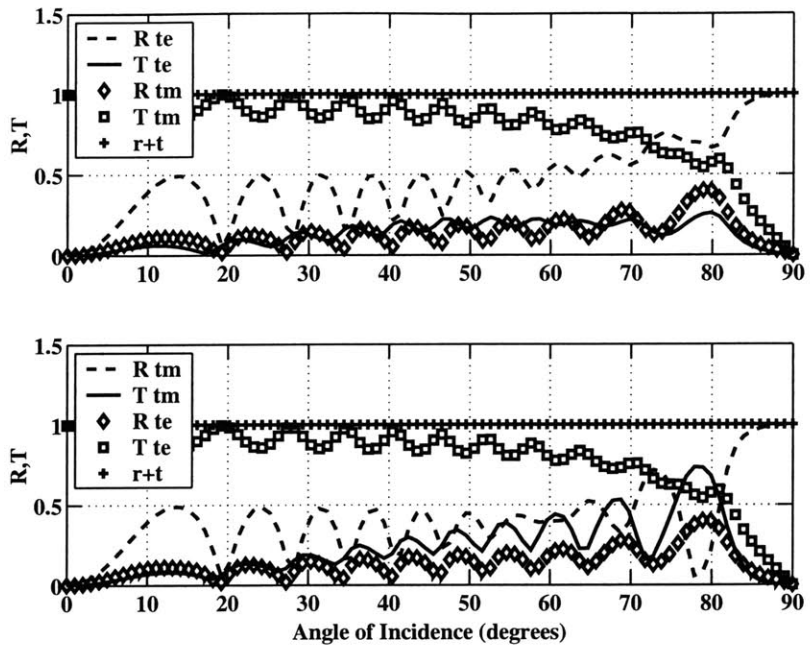

Figure 3-5: **Fresnel coefficients for non-lossy uniaxial slab**($n_0 = 1.5, n_e = 2, \phi = 45^o$)

$$b_{2x} = (\kappa_{11} he_{2y} k_{ez} + \kappa_{12}(he_{2z} k_x - he_{2x} k_{ez}) - \kappa_{13} k_x he_{2y})$$
$$a_{1y} = (-\kappa_{21} ho_{1y} k_{oz} + \kappa_{22}(ho_{1x} k_{oz} + ho_{1z} k_x) - \kappa_{23} k_x ho_{1y})$$
$$b_{1y} = (-\kappa_{21} he_{1y} k_{ez} + \kappa_{22}(he_{1x} k_{ez} + he_{1z} k_x) - \kappa_{23} k_x he_{1y})$$
$$a_{2y} = (\kappa_{21} ho_{2y} k_{oz} + \kappa_{22}(ho_{2z} k_x - ho_{2x} k_{oz}) - \kappa_{23} k_x ho_{2y})$$
$$b_{2y} = (\kappa_{21} he_{2y} k_{ez} + \kappa_{22}(he_{2z} k_x - he_{2x} k_{ez}) - \kappa_{23} k_x he_{2y})$$
$$a_{1z} = (-\kappa_{31} ho_{1y} k_{oz} + \kappa_{32}(ho_{1x} k_{oz} + ho_{1z} k_x) - \kappa_{33} k_x ho_{1y})$$
$$b_{1z} = (-\kappa_{31} he_{1y} k_{ez} + \kappa_{32}(he_{1x} k_{ez} + he_{1z} k_x) - \kappa_{33} k_x he_{1y})$$
$$a_{2z} = (\kappa_{31} ho_{2y} k_{oz} + \kappa_{32}(ho_{2z} k_x - ho_{2x} k_{oz}) - \kappa_{33} k_x ho_{2y})$$
$$b_{2z} = (\kappa_{31} he_{2y} k_{ez} + \kappa_{32}(he_{2z} k_x - he_{2x} k_{ez}) - \kappa_{33} k_x he_{2y})$$

Solving these, we obtain the reflection and transmission coefficients (Fresnel coefficients) for of the slab for TM incidence. Figure 3-6, shows the Fresnel's coefficients for a non-lossy uniaxial slab, for both TE and TM incidences, when the incidence is in the x-z plane ($\phi = 0$). As can be observed, both the reflection as well as the transmission coefficients have both TE and TM components in each case, the amplitudes of all of which add up to unity.

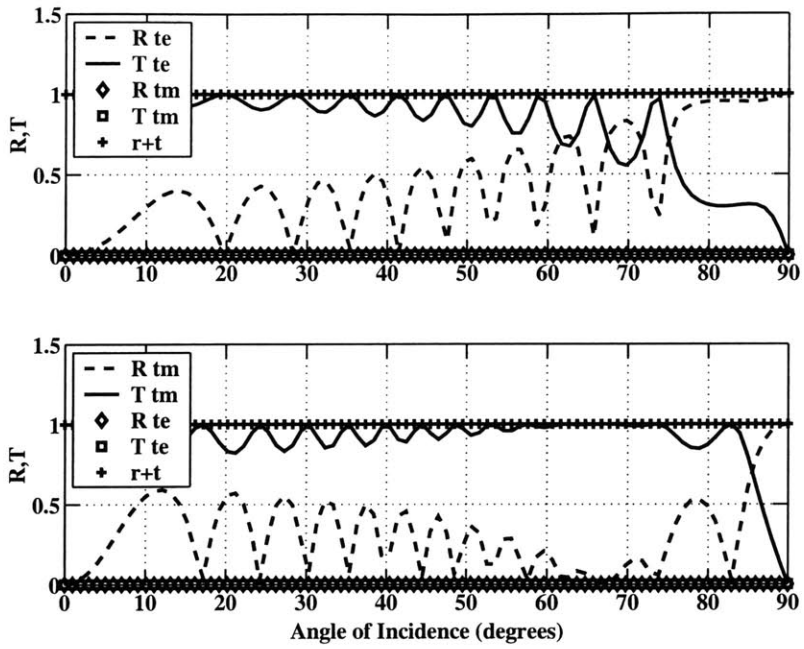

Figure 3-6: **Fresnel coefficients for non-lossy uniaxial slab** $(n_0 = 1.5, n_e = 2, \phi = 0)$

Thus we have developed the general formulation to obtain the Fresnel's coefficients of an uniaxial slab for any incidence.

3.4 Analysis of Different Types of Polarizers

We now study the performance characteristics of different types of polarizers using the formulations we have developed in the previous sections. As has been previously mentioned, we aim at studying: 1. Leakage through crossed polarizers and 2. Transmission coefficients of single polarizers. We analyse three broad classes of polarizers, which are : 1. O-type polarizers, 2. E-type polarizers, and 3. O-type and E-type metamaterial polarizers. Table3.1. shows the ordinary and extraordinary refractive indices of the polarizers under consideration. The O-type [3] and E-type [4] values in Table 3.1, are the typical values of refractive indices of polarizers in practise today. Whereas, the values for the metamaterial polarizers are those that are feasible with currently available materials and polarizer manufacturing technologies.

Polarizer	n_o	n_e
O-Type	1.5	1.5+0.03i
E-Type	1.5+0.03i	2.1
Metamaterial O-Type	2	2i
Metamaterial E-Type	2i	2

Table 3.1: **Different Types of Polarizers**

3.4.1 Leakage through crossed polarizers

Leakage through crossed polarizers is of significant concern in optical applications, and has been widely studied. Yeh (1993) has given detailed analysis of leakage through crossed O-type polarizers based on Jones matrix formulation. Yeh (1993) and Lazarev and Paukshto (2001) have also given explicit analytical expressions for leakage through O-type as well as E-type polarizers, i.e for T_o and T_e. In the present study, as mentioned in Section 3, we have obtained the ordinary and extraordinary wave vectors using the kDB method, and used the relations in [5] to obtain T_o and T_e for the different polarizers using the kDB method presented earlier.

Figure 3-7 shows a plot of leakage versus incident angle for conventional O-type polarizers versus E-type polarizers. The plot conforms with that presented in [5], where it was demonstrated that E-type polarizers have lesser leakage (T_e) than O-type polarizers (T_o), if the n_o of the O-type is less than or equal to the lesser of the n_o and n_e of the E-type polarizer.

It is important to note that the condition n_o(O-type) $\leq \min[n_o, n_e]$ (E-type) is usually satisfied because it has recently been possible to fabricate E-type polarizers that have much higher refractive indices as compared to conventional O-type polarizers [4]. It is therefore pertinent to note that, inorder to see any improvement beyond the performance of the present E-type polarizers, we need to have either novel O-type polarizers with n_o values higher than their conventional counterparts, or E-type polarizers with n_e values higher than those prevalent in practise today. These requirements can be met using metamaterial polarizers.

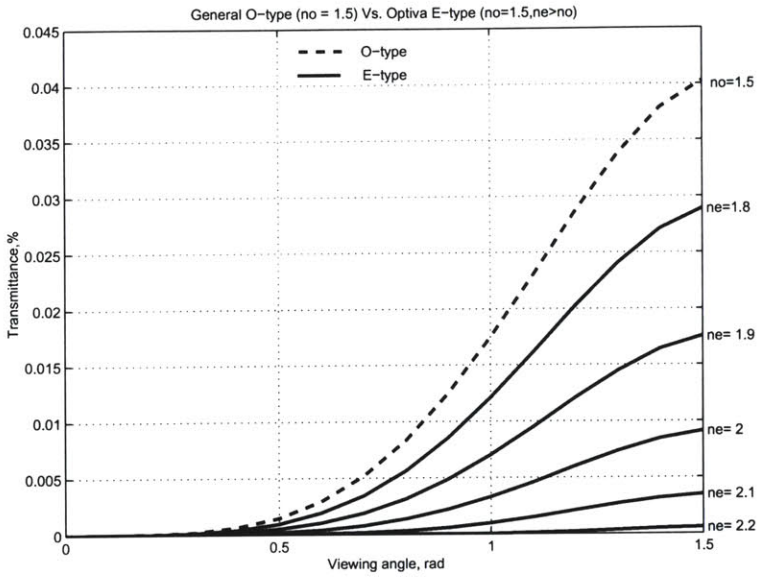

Figure 3-7: **Leakage in O-type versus E-type polarizers**

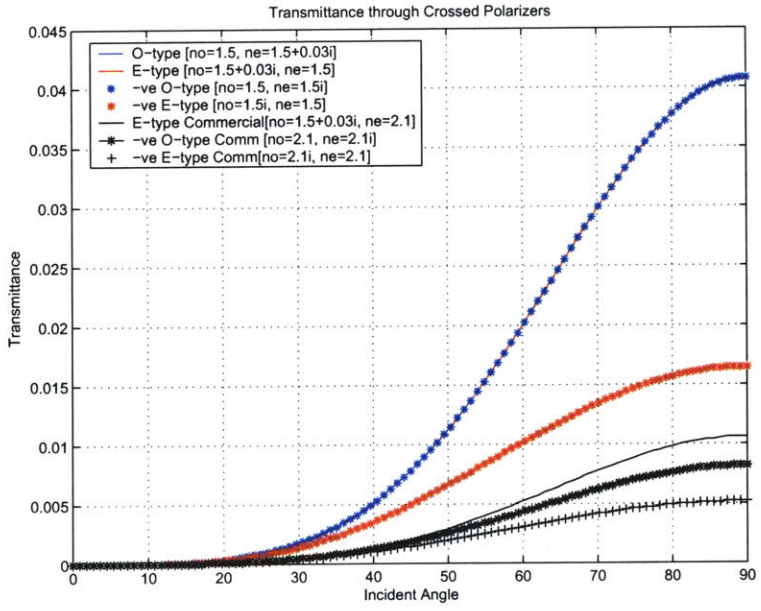

Figure 3-8: **Leakage in different types of polarizers**

Metamaterial polarizers can be obtained by doping metallic nano-needles in an isotropic, homogeneous background. The refractive indices of metamaterial polarizers are based on the refractive index of the background material. By suitable choice of material, the background medium can be made up of high refractive index, leading to a high refractive index polarizer. The values of the refractive indices of the metamaterial polarizers in Table 3.1, reflect this advantage.

Figure 3-8 shows a plot of leakage versus incident angle for the different polarizeres listed in Table 1. It can be observed that the leakage is least for the O-type metamaterial polarizer as expected.

3.4.2 Transmission coefficients

The transmission coefficients for the different polarizers for TE and TM incidences are obtained using the formulation in Section 3. Each polarizer is considered as an uniaxial slab with the optic axis along the x-axis, and the normal being along the z-axis. The slab thickness is 13 times the wave length. The wavelength under consideration is 0.5 microns which is in the optical range. The incident wave vector is considered to be in the x-z plane ($\phi = 0$ and $\theta \in [0, \pi/2]$), so as to obtain the maximum possible transmission. For non-normal incidence, the TE and TM components of the transmitted and reflected waves are coupled. Therefore, for TE incidence there are both TE and TM components of the reflection and transmission coefficients (Fresnel coefficients), and same for TM incidence.

Figure 3-9 shows the plot of the Fresnel coefficients versus incident angle, for a conventional O-type polarizer, with the ordinary and extraordinary refractive indices, $n_o = 1.5$ and $n_e = 1.5 + 0.03$i. It can be observed that for TE incidence, there is near perfect transmission of the TE component, i.e there is no attenuation (apparent from the fact that the normalized transmitted and reflected powers add up to unity). However, for TM incidence, there is no transmission, owing to the fact that the wave is completely attenuated. It is important to note that the transmitted power is near

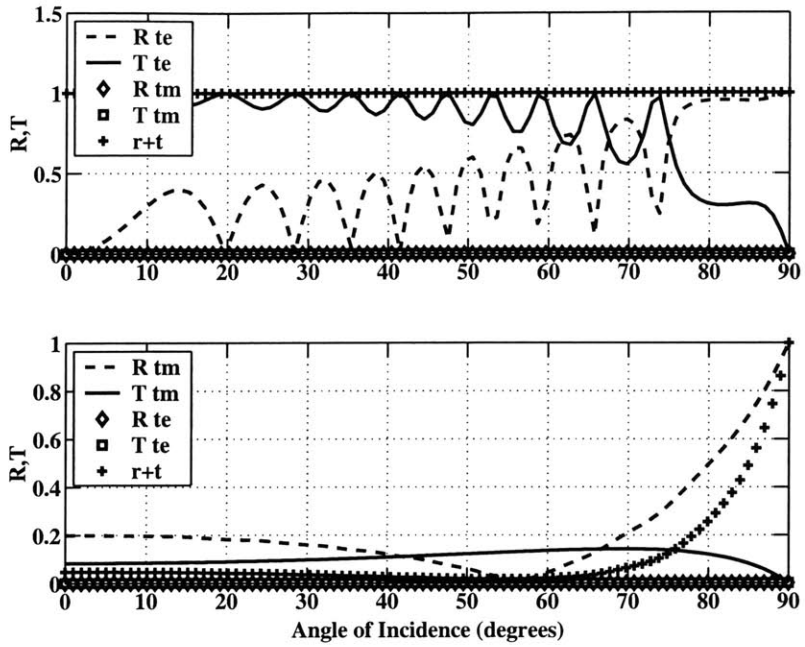

Figure 3-9: **Fresnel coefficients for an O-type polarizer**($n_0 = 1.5, n_e = 1.5 + 0.03i, \phi = 0$)

unity for most of the incident angles, and decreases to zero for grazing incidence.

Figure 3-10 shows the plot of the Fresnel coefficients for an E-type polarizer, with n_o = 1.5+0.03i and n_e = 2.1, as mentioned in Table 3.1. The two parts of the figure show plots for TE incidence and TM incidence respectively. It can be observed that for TE incidence, there is no transmission of the TE component, as could be expected. However, for TM incidence one would expect to obtain near perfect transmission of the TM component. It can be seen from the figure that perfect transmission is obtained only for near normal incidence. Where as, for other angles of incidence the TM wave is monotonically attenuated until it completely diminishes at grazing incidence. This leads to a significant loss of incident power for non-normal angles of incidence.

Figure 3-11 and Figure 3-12 show the plots for metamaterial polarizers, with refractive indices shown in Table 3.1. Figure 3-11, for the O-type metamaterial polarizer, shows a plot very similar to Figure 3-9. For TE incidence, there is near perfect transmission of the TE component for a wide range of incident angles, where as for TM incidence there is no transmission. Figure 3-12 shows the plot for the E-type

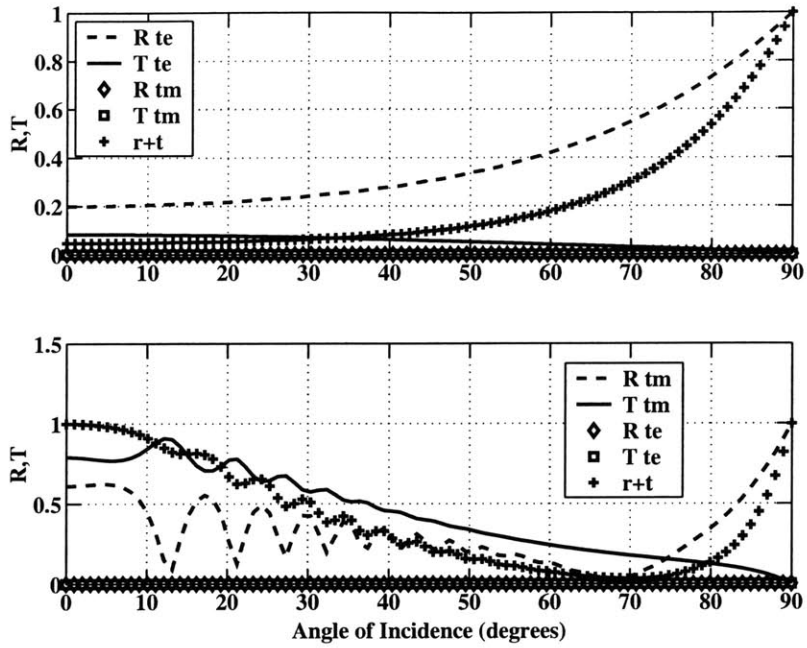

Figure 3-10: **Fresnel coefficients for an E-type polarizer**($n_0 = 1.5 + 0.03i, n_e = 2.1, \phi = 0$)

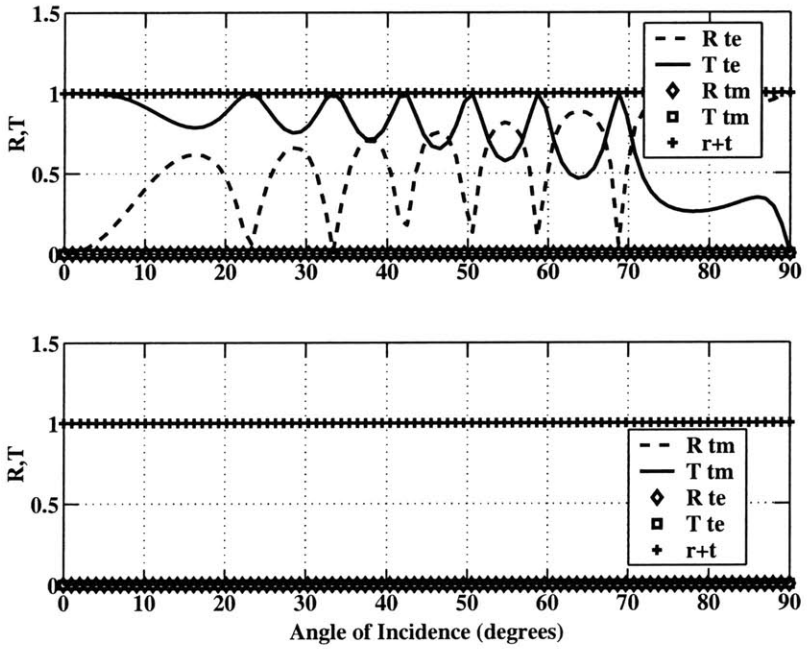

Figure 3-11: **Fresnel coefficients for an O-type Metamaterial polarizer**($n_0 = 2, n_e = 2i, \phi = 0$)

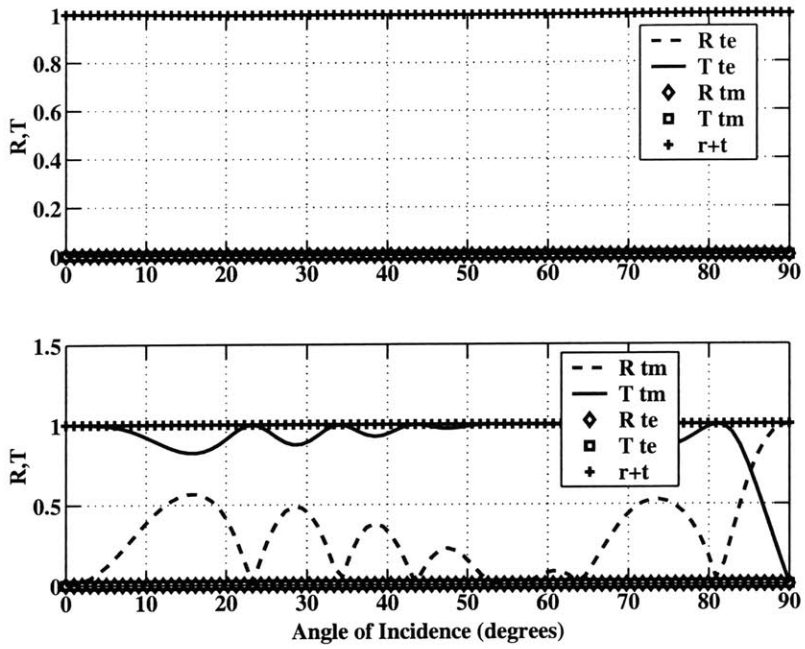

Figure 3-12: **Fresnel coefficients for an E-type Metamaterial polarizer**($n_0 = 2i, n_e = 2, \phi = 0$)

metamaterial polarizer. As can be observed, for TM incidence there is near perfect transmission, where as the TE component of the incident wave is completely attenuated. It is important to note here that the transmission of the TM component is near perfect for almost all angles of incidence, vanishing only at near grazing incidence.

Thus, the transmitted power for an O-type metamaterial polarizer is comparable to that of a conventional polarizer, whereas the transmitted power for a conventional E-type polarizer is less than that of O-type and E-type metamaterial polarizers as well as the conventional O-type polarizers, for non-normal incidence.

From the above observations on leakage and transmission properties of the various polarizers, it can be noted that an O-type metamaterial polarizer would have better performance characteristics than the remaining ones. This is because, it shows minimum cross-polarizer leakage and maximum possible transmission.

Chapter 4

Conclusions

4.1 Radiation Mechanism of S - shaped SRR

In the present study the radiation phenomenon in Left-Handed Media is thoroughly studied. The S-shaped SRR is one of the most recent advancements in the area of LHM theory, and it allows great convenience in the analysis of the current modes along the structure. Therefore, this structure formed the basis of the radiation analysis presented here. The structure was simulated in a wave-guide set-up, with Perfect Electric Conductor (PEC) and Perfect Magnetic Conductor (PMC) boundaries. These idealizations allowed the propagation of a TEM mode in a rectangular waveguide. With the geometry of the set-up as discussed before, and the TEM incidence, an effective LHM was realized using the S-structures.

The simulations were conducted using the Ansoft HFSS Electromagnetic solver. The solutions enabled calculation of the surface current densities on the S rings. By simulating a set-up with three SRRs in the wave-propagation direction, the phase difference between adjacent SRRs was determined. This progressive phase increment was found to be negative, thereby suggesting a backward wave which is the characteristic of an LHM.

The currents on the rings were expanded into a Fourier series using the Fast Fourier Transform algorithm. It was found that only one current mode was dominant. This mode was used to obtain the vector current moment due to one SRR. A generalized

formulation was developed to determine the array factor of an arbitrary array. The formulation was used to obtain the radiation pattern of a prism of S rings, using only the edge elements and the progressive phase obtained from HFSS simulations. The radiation pattern confirmed negative refraction behavior of the structure.

4.2 Polarizing Properties of Uniaxial Metamaterials

The polarizing characteristics of a metamaterial polarizer that has a uniaxial permittivity tensor with a negative permittivity along the optic axis and a positive isotropic permeability, were studied. A comparison was made between existing polarizers and a metamaterial polarizer. The comparison was based on (1) Leakage of light (transmittance) through a pair of crossed-polarizers, and (2) Fresnel coefficients of a single polarizer.

It was observed that metamaterials allow lesser leakage of unpolarized light as compared to any other polarizer. This is primarily because having only ϵ negative causes a large imaginary refractive index, leading to greater attenuation and hence lesser leakage.

A general formulation based on the kDB method was developed to study wave propagation through uniaxial media. The Fresnel coefficients of the difference types of polarizers were obtained and compared. It was observed that metamaterials have maximum transmission and least leakage as compared to the other polarizers.

Bibliography

[1] John B. Pendry and David R. Smith, Light With Negative Refraction, Physics Today, June 2004.

[2] J. A. Kong, Electromagnetic Wave Theory, EMW Publishing, Cambridge, MA, pp. 305-404 (2000).

[3] V. G. Veselago, Soviet Physics USPEKI, Vol. 10, No.509 (1968).

[4] D. Pines and D. Bohm, Phys. Rev., Vol. 85, No. 2, pp. 338 (1952).

[5] D. Bohm and D. Pines, Phys. Rev., Vol. 92, No. 3, pp. 609 (1953).

[6] J. B. Pendry, A. J. Holden, W. J. Stewart, I. Youngs, Phys. Rev. Lett., Vol. 76, pp. 4773 (1996).

[7] J. B. Pendry, A. J. Holden, D. J. Robbins and W. J. Stewart, Journal of Physics: Condensed Matter, Vol. 10, pp. 4785 (1998)

[8] J. B. Pendry, A. J. Holden, D. J. Robbins, and W. J. Stewart, IEEE Trans. on Microwave Theory and Tech., Vol. 47, No. 11, pp. 2075 (1999).

[9] R. A. Shelby, D. R. Smith, S. Schultz, Science, Vol 292, pp. 77 (2001).

[10] A. A. Houck, J. B. Brock, I. L. Chuang, Phys. Rev. Lett., Vol. 90, pp. 137401 (2003)

[11] C. R. Simovski and B. Sauviac, RADIO SCIENCE, Vol. 39, pp. RS2014 (2004).

[12] Hongsheng Chen, Lixin Ran, Jiangtao Huangfu, Xianmin Zhang, Kangsheng Chen, Tomasz M. Grzegorczyk, Jin Au Kong. (Internal Communication on S-shaped Split-ring Resonator)

[13] M. Paukshto, E-type Polarizers and Their Applications, SID Bay Area Chapter Seminar, CA (2001).

[14] P. Yeh, C. Gu, "Optics of Liquid Crystal Displays", John Wiley and Sons,Inc.,USA, (1999) .

[15] P. Yeh and M. Paukshto "Extraordinary polarizers for LCD", White Paper, Optiva Inc.,CA (2000).

[16] N. Madhusudhan, Tomasz M. Grzegorczyk, Bae-Ian Wu, Joe Pacheco and J. A. Kong, Progress in Electromagnetic Research Symposium, Honolulu, Hawaii, (2003).

[17] Xudong Chen, Tomasz M. Grzegorczyk, Bae-Ian Wu, Joe Pacheco Jr., and Jin Au Kong, Phy. Rev. E, Vol. 70, pp. 016608 (2004).

[18] D. R. Smith, D. C. Vier, N. Kroll, and S. Schultz, Applied Physics Letters, Vol. 77, No. 14, pp. 2246 (2000)

[19] D. R. Smith, S. Schultz, P. Markos, and C. M. Soukoulis, Phys. Rev. B, Vol. 65, pp. 195104 (2002).

[20] P. Markos and C. M. Soukoulis, Optics Express, Vol. 11, pp. 649 (2003).

[21] Christopher Moss, Ph.D. Thesis, Massachusetts Institute of Technology (2004)